

Initial conditions of star formation at $\lesssim 2000$ au: physical structure and NH_3 depletion of three early-stage cores

Y. Lin¹, S. Spezzano¹, J. E. Pineda¹, J. Harju², A. Schmiedeke³, S. Jiao⁴, H. B. Liu⁵, and P. Caselli¹

¹ Max-Planck-Institut für Extraterrestrische Physik, Giessenbachstr. 1, D-85748 Garching bei München, Germany
e-mail: ylin@mpe.mpg.de

² Department of Physics, P.O. Box 64, FI-00014, University of Helsinki, Finland

³ Green Bank Observatory, PO Box 2, Green Bank, WV 24944, USA

⁴ National Astronomical Observatories, Chinese Academy of Sciences, Beijing 100101, China

⁵ Department of Physics, National Sun Yat-Sen University, No. 70, Lien-Hai Road, Kaohsiung City 80424, Taiwan, R.O.C.

Received ; accepted

ABSTRACT

Context. Pre-stellar cores represent a critical evolutionary phase in low-mass star formation. Characterisations of the physical conditions of pre-stellar cores provide important constraints to star and planet formation theory, and are pre-requisite for establishing the dynamical evolution and the related chemical processes.

Aims. We aim to unveil the detailed thermal structure and density distribution of three early-stage cores, starless core L1517B, and prestellar core L694-2 and L429, with the high angular resolution observations of the NH_3 (1,1) and (2,2) inversion transitions obtained with VLA and GBT. In addition, we explore where/if NH_3 depletes in the central regions of the cores.

Methods. We calculate the physical parameter maps of gas kinetic temperature, NH_3 column density, line-width and centroid velocity of the three cores, utilising the NH_3 (1,1) and (2,2) lines. We apply the mid-infrared extinction method to the *Spitzer* $8\mu\text{m}$ map to obtain a high angular resolution hydrogen column density map. We examine the correlation between the derived parameters, and the properties of individual cores. We derive the gas density profile from the column density maps and assess the variation of NH_3 abundance as a function of gas volume density.

Results. The measured temperature profiles of the cores L429 and L1517B show a minor decrease towards the core center, dropping from ~ 9 K to below 8 K, and ~ 11 K to 10 K, while L694-2 has a rather uniform temperature distribution around ~ 9 K. Among the three cores, L429 has the highest central gas density, close to sonic velocity line-width, and largest localised velocity gradient, all indicative of an advanced evolutionary stage. We resolve that the abundance of NH_3 becomes 2 times lower in the central region of L429, occurring around a gas density of $4.4 \times 10^4 \text{ cm}^{-3}$. Compared to Ophiuchus/H-MM1 (Pineda et al. 2022) which shows an even stronger drop of the NH_3 abundance at $2 \times 10^5 \text{ cm}^{-3}$, the abundance variations of the three cores plus Ophiuchus/H-MM1 suggest a progressive NH_3 depletion with increasing central density in pre-stellar cores.

Key words. ISM: pre-stellar core – ISM: L429, L694-2, L1517B – ISM: structure – stars: formation

1. Introduction

Pre-stellar cores represent a critical stage in the process of low-mass star formation: the molecular gas has reached adequate density for self-gravity to balance or even surpass the outward forces (thermal and turbulent pressure, rotation and magnetic field, see e.g. Myers & Benson 1983, Bergin & Tafalla 2007, Pineda et al. 2023). Compared to its prior stage of starless cores, these cores are denser and at the verge of forming protostars. The significance of studying the physical conditions of pre-stellar cores is twofold: (1) it sheds light on the physical mechanisms at play in the imminence of star formation (Keto & Caselli 2010, Keto et al. 2015), (2) it provides essential constraints on understanding the chemical processes that influence the properties of gas and dust at a critical phase of interstellar medium evolution (Caselli & Ceccarelli 2012).

Along with the special physical status, pre-stellar cores are characterised by strong molecular depletion including accretion/freezing onto dust grains, and appear chemically distinctive to the preceding and more evolved core phases. The strong molecular freeze-out enhances the deuterium fractionation, e.g., deuterated isotopologues of NH_3 can form through reactions of

NH_3 with deuterated ions in the gas phase (Rodgers & Charnley 2001, Roueff et al. 2005, Sipilä et al. 2015), the process of which also affects the abundance of NH_3 , composing another source of NH_3 depletion. However, among various molecules, nitrogen-bearing species (e.g., N_2H^+ , NH_3) show relative longevity in the gas (Caselli et al. 1999, Caselli et al. 2002b, Aikawa et al. 2005, Flower et al. 2006, Bergin & Tafalla 2007, Sipilä et al. 2015) and have been important molecular tracers of the inner core region (e.g., Bergin et al. 2006; Friesen et al. 2009; Pineda et al. 2010, 2011; Chitsazzadeh et al. 2014; Pineda et al. 2015). While previous observations show marginal evidence that ammonia depletion happens at very high gas densities (e.g., Tafalla et al. 2004, Crapsi et al. 2005), recent work based on the deep interferometric observations towards pre-stellar core Ophiuchus/H-MM1 (hereafter H-MM1) uncover direct evidence that NH_3 depletes already at a few times 10^5 cm^{-3} (Pineda et al. 2022); this showcases the necessity of high angular observations for revealing the depletion of NH_3 and further elucidating the chemical properties related to NH_3 formation, e.g., the volatility of atomic and molecular nitrogen.

The inversion transitions of NH_3 in metastable rotational levels are an important thermometer for dense gas (Ho & Townes

1983, Walmsley & Ungerechts 1983), making ammonia a valuable tracer for molecular clouds. Towards low-mass cores in particular, NH_3 is a reliable tracer of line-of-sight mass averaged temperature (Juvela et al. 2012), when the cores can be approximated by a $\sim 1 M_\odot$ Bonnor-Ebert sphere without being too opaque. Due to photo-electric heating, high-density ($\sim 10^5 \text{ cm}^{-3}$) starless cores immersed in interstellar radiation field are predicted to exhibit a gas temperature increase toward the core edge (Galli et al. 2002). Based on measurement of NH_3 lines, while some starless cores have a rather constant gas temperature profile (variations of $\lesssim 1 \text{ K}$, Tafalla et al. 2004, Ruuskanen et al. 2011, Chitsazzadeh et al. 2014, Spear et al. 2021), centrally decreasing temperature profile has been revealed towards a handful of starless and pre-stellar cores (Hotzel et al. 2001, Crapsi et al. 2007, Pagani et al. 2007, Harju et al. 2017, Pineda et al. 2022). In particular, Crapsi et al. 2007 unveil a remarkable temperature drop down to $\sim 6 \text{ K}$ inside a late-stage pre-stellar core L1544. This deviation from isothermality and the corresponding varying core density conform with an evolutionary view for starless cores immediately prior to protostar formation (Evans et al. 2001, Zucconi et al. 2001, Keto & Field 2005, Keto & Caselli 2008a).

In this work, we utilise high angular resolution NH_3 (1,1) and (2,2) observations of one starless core L1517B and two pre-stellar cores L694-2 and L429, to investigate the physical conditions and the variations of NH_3 abundance in pre-stellar cores. We adopt mid-infrared extinction methods to characterise the density structure of the three cores, achieving a similar angular resolution of $5''$ with the NH_3 observations to allow a direct comparison. This enables us to provide a detailed picture of temperature and density distribution, and the NH_3 abundance mapping of the three cores.

In Sect. 2 we describe the observations, data reduction and combination procedure. Sect. 3.1 -3.2 detail the calculation of hydrogen column density maps with extinction methods, and the derived radial density profiles. In Sect. 3.3-3.4 we elaborate on the fitting procedure of the NH_3 lines and present the obtained parameter maps. In Sect. 4 we compare the derived physical parameters of the three cores, focusing primarily on the thermal structure and the NH_3 abundance variations.

2. Observations and data reduction

The K -band, single-pointing NH_3 (1,1) and (2,2) image cubes of the three cores (Table 1, more in Appendix A) were taken with the Jansky Very Large Array (JVLA) in 2013 (Project ID: 13A-394, PI: S. Chitsazzadeh). The JVLA correlator was configured to use the 8-bit sampler and two basebands, of 8 MHz bandwidth and 2048 channels in dual polarisation mode, achieving a velocity resolution of 0.05 km s^{-1} . The quasars 3C286 and 3C48 are used as the flux and passband calibrators, and J1743-0350, J1925+2106, J0414+3418 as phase calibrators for the target sources L429, L694-2 and L1517B, respectively. The raw data was calibrated with the pipeline of Common Astronomy Software Applications (CASA) version 6.2.1. Single-dish data was obtained additionally from the Green Bank Telescope (GBT) using the K -band Focal Plane Array (KFPA), achieving an angular resolution of $\sim 33''$ (Project ID: GBT10B-020, GBT10C-055, GBT11A-052, PI: S. Chitsazzadeh). The raw data was reduced with the GBT pipeline.

We utilise a hybrid method for combining the VLA and GBT data, following the procedure elaborated in Liu et al. (2015)¹

¹ <https://github.com/baobabyoo/al mica>

and used by e.g., Monsch et al. (2018), Lin et al. (2022), which is based on imaging tasks provided in the *miriad* software (Sault et al. 1995). The procedure consists of two essential parts: generating pseudo-visibility from the single-dish data with *uvrandom* and *uvmodel* tasks, and joint deconvolution of the pseudo-visibility with the interferometric visibilities to obtain a clean datacube; the datacube is further merged with the single-dish data with *immerge* task, to preserve the total flux. The following analysis and results are based on the final datacubes produced by this combination method. With the *invert* task in joint deconvolution step, we apply a taper function to obtain a gaussian beam of $\sim 5''$ for the data cubes, which is preserved after *immerge*.

We additionally adopt the combination method elaborated in Pineda et al. (2022) which is essentially a model-assisted deconvolution procedure of the interferometric data. The Common Astronomy Software Applications (CASA) software is used for this approach. Specifically, the single-dish data is used as a *startmodel* in *tclean* to facilitate image reconstruction of the VLA data. This combination method essentially adopts the single-dish image as prior information to model the missing extended emission solely from the interferometry-only constraints. We use multi-scale deconvolution algorithm with natural weighting and a common restoring beam of $5''$ after applying *uvtaper*. The *scales* parameter is set to be $0''$, $5''$, $15''$ and $45''$, reflecting the typical size scales of dominant image features. As a final step, we use *feather* to add this model-assisted deconvolved datacube with the single-dish data, obtaining the final data products.

Both methods yield a final datacube regridded to a channel width of 0.1 km s^{-1} . The achieved noise level is $\sim 3 \text{ mJy beam}^{-1}$ per channel. We compare the obtained NH_3 column density of the two data products in Appendix C, which shows that the analysis is not biased by the different combination methods, for a robust comparison with the results in Pineda et al. (2022).

Table 1. The observed cores.

Source	R.A. (J2000)	Dec. (J2000)	v_{LSR} (km s^{-1})	Distance ^a (pc)
L694-2	19:41:04.5	+10:57:02.0	9.5	203
L429	18:17:05.8	-08:14:05.3	6.7	436
L1517B	04:55:18.3	+30:37:47.0	5.8	159

^a The distance references are Kim et al. (2022), Ortiz-León et al. (2018), and Galli et al. (2019).

3. Results

3.1. H_2 column density maps from Spitzer $8 \mu\text{m}$

Owing to high column densities of cold dust, pre-stellar cores often appear as dark structures on mid-infrared surface brightness maps. Following the mid-infrared extinction calculations elaborated in Harju et al. (2020), we adopted the $850 \mu\text{m}$ emission map observed by SCUBA-2²³ and the $250 \mu\text{m}$, $350 \mu\text{m}$

² <https://www.cadc-ccda.hia-ihc.nrc-cnrc.gc.ca/en/jcmt/>

³ The James Clerk Maxwell Telescope is operated by the East Asian Observatory on behalf of The National Astronomical Observatory of Japan; Academia Sinica Institute of Astronomy and Astrophysics; the Korea Astronomy and Space Science Institute; the National Astronomical Research Institute of Thailand; Center for Astronomical Mega-Science (as well as the National Key R&D Program of China with

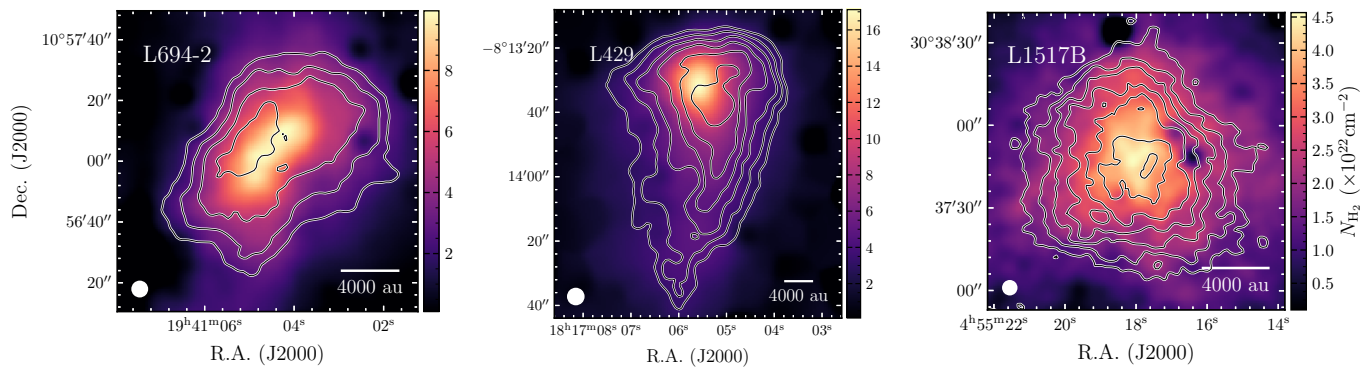


Fig. 1. Hydrogen column density maps ($N(\text{H}_2)$) derived from *Spitzer* $8\mu\text{m}$ extinction. The contours show the integrated intensity map of the main component of NH_3 (1,1) line. The void regions in L694-2 and L1517B of very low $N(\text{H}_2)$ correspond to nearby bright point $8\mu\text{m}$ sources. The beam size is indicated as a white filled circle in each figure. For L694-2 and L429 the contours start from 1 K km s^{-1} and 1.5 K km s^{-1} , respectively, with a spacing of 0.5 K km s^{-1} . For L1517B the contours start from 0.5 K km s^{-1} with a spacing of 0.3 K km s^{-1} .

and $500\mu\text{m}$ emission maps⁴ from the *Herschel*/SPIRE telescope⁵ (Griffin et al. 2010) to facilitate the derivation of the high angular resolution, hydrogen column density maps ($N(\text{H}_2)$) from the *Spitzer*/IRAC $8\mu\text{m}$ data.

With a modified black-body emission model, we first employed *Herschel*/SPIRE maps to derive a dust temperature map (T_{dust}) at $\sim 21''$ resolution (with the high angular resolution SPIRE maps in the archive) from Spectral Energy Distribution (SED) fitting. The temperature map is later used to derive the dust opacity map at $850\mu\text{m}$ ($\tau_{850\mu\text{m}}$). We adopted dust emissivities for unprocessed (not coagulated) dust grains with thin ice mantles from Ossenkopf & Henning (1994) (OH4 model); in this model, the dust emissivities in the submm regime can be approximated by a power-law form with index of $\beta = 2.0$ with a reference value for the cross section per unit mass of gas at $850\mu\text{m}$, $\kappa_{850\mu\text{m}}$, of $0.011\text{ cm}^2\text{ g}^{-1}$, adopting a gas-to-dust mass ratio of 100. The corresponding $\kappa_{8\mu\text{m}}$ is $8.85\text{ cm}^2\text{ g}^{-1}$. With this assumption, we neglect the change in dust emissivities in the cores due to the possibly varying dust grain properties. For example, the $\kappa_{8\mu\text{m}}/\kappa_{850\mu\text{m}}$ decrease with coagulation with increasing gas densities and the formation of ice mantles, which is likely happening in the innermost, denser region of these pre-stellar cores (e.g., Bergin et al. 2006, Chacón-Tanarro et al. 2017, 2019). We discuss possible bias and hints for dust opacity variations below and in Appendix D.

The mid-infrared extinction calculation in Harju et al. (2020) adopts the $\tau_{850\mu\text{m}}$ map to estimate the foreground (and zero point correction) and background emission level for the $8\mu\text{m}$ map. Specifically, the $8\mu\text{m}$ map is first masked out of the regions of high $\tau_{850\mu\text{m}}$ (area of dense core) and of high $8\mu\text{m}$ emission level (compact bright sources). The background image is then constructed by linearly interpolating over the masked regions using triangulation. For a relatively uniform $8\mu\text{m}$ emission field this method produces a rather smooth background image. In case of highly locally varying $8\mu\text{m}$ field, e.g., with bright compact sources immersed in relatively strong large-scale emission showing low contrast between spatial scales, the masking of bright sources based on constant threshold can cause visible defect to

the interpolated background image. We therefore also adopt the small-scale median filter method (Butler & Tan 2009) to estimate the emission background, which first effectively smooths out the local inhomogeneity and then conducts interpolation for the masked region. The detailed procedure is elaborated in Appendix D. At any rate, the process of background estimation is subject to the difficulty of distinguishing between small-scale background emission variations and the genuine absorbing components (Butler & Tan 2009).

Estimation of the foreground emission level I_{fg} is guided by the dust opacity map obtained from SED fitting. The foreground emission is assumed to be spatially constant and is estimated in an iterative way such that the resultant peak $\tau_{8\mu\text{m}}$ after smoothing achieves better consistency with that predicted by SED, adopting the dust opacity relations mentioned before. Naturally, the upper limit of I_{fg} of the extinction method is the minimum flux level toward the core center, i.e. when the core absorbs all the background emission and that the observed flux solely comes from the foreground emission.

Although the $\tau_{850\mu\text{m}}$ is of higher angular resolution compared to opacity maps from *Herschel* data, lack of extended emission inherent to ground-based bolometric observations of SCUBA2 can easily result in underestimates of the true column densities, which is not necessarily only affecting the extended region of the core. In our specific case, the $850\mu\text{m}$ emission maps available for the two cores L429 and L694-2 are also rather shallow, achieving an rms level of $\sigma \sim 0.15\text{ mJy/arcsec}^{-2}$ (mass sensitivity per beam corresponds to $0.05 M_{\odot}$ for a source at 200 pc of temperature 10 K). To improve the quality of the SCUBA2 $850\mu\text{m}$ emission map and preserve the extended emission, we resort to a continuum combination method applicable to emission maps obtained from ground-based bolometers and space telescopes, which is first proposed by Liu et al. 2015, and further developed in Jiao et al. (2022). We utilised the PLANCK 353 GHz ($\lambda = 850\mu\text{m}$) continuum data for compensating the extended structures; the PLANCK image was first deconvolved with a model image of extrapolated $850\mu\text{m}$ emission from the SED of the *Herschel* maps. We give a brief summary of the method in Appendix B.

After obtaining a combined $850\mu\text{m}$ image (Fig. B.1), we derived a $14''$ $N(\text{H}_2)$ map by applying the T_{d} map to the $850\mu\text{m}$ flux. This $N(\text{H}_2)$ is relatively free of unexpected uncertainties compared to the high resolution $N(\text{H}_2)$ derived from extinction method. With the assumed dust opacity values, the peak from the derived $\tau_{8\mu\text{m}}$ should match that predicted by $\tau_{850\mu\text{m}}$

No. 2017YFA0402700). Additional funding support is provided by the Science and Technology Facilities Council of the United Kingdom and participating universities and organizations in the United Kingdom and Canada.

⁴ We adopt the level 2.0 processed data products; the observational ID (OBSID) for L694-2 is 1342230846, for L429 is 1342239787, and for L1517B is 1342204843/1342204844.

Table 2. Density profile parameters from fitting the $N(\text{H}_2)$ map derived from $8\ \mu\text{m}$ extinction.

Source	n_c ($10^5\ \text{cm}^{-3}$)	r_{flat} (au)	R^a (pc)	Mass ^b (M_\odot)
L694-2	8.3(0.2)	2700(100)	0.1	8.3
L429	9.5(0.5)	4000(400)	0.1	4.0
L1517B	3.2(0.1)	3200(100)	0.1	2.0

^a The maximum outer radius R in the fits is set to 0.10 pc for all three cores.

^b The total mass is calculated within a common radius of 0.05 pc.

Uncertainties of parameter n_c and r_{flat} are listed in parentheses as absolute values.

map ($\tau_{8\ \mu\text{m}, 850\ \mu\text{m}}^{\text{pred}} = \tau_{850\ \mu\text{m}} \frac{\kappa_{8\ \mu\text{m}}}{\kappa_{850\ \mu\text{m}}}$). For L1517B which lacks SCUBA2 measurements, we instead use the $\tau_{250\ \mu\text{m}}$ to gauge the $\tau_{8\ \mu\text{m}}$. Practically, we find that even if we set the foreground emission level to be the lowest flux level of the $8\ \mu\text{m}$, the derived peak $\tau_{8\ \mu\text{m}}$ is lower than that predicted based on $\tau_{850\ \mu\text{m}}$ (or $\tau_{250\ \mu\text{m}}$ in the case of L1517B). This is likely due to (1) underestimate of background level based on the interpolation method (2) possible variations of dust opacity values in the center of the core. Comparing the extended regions of the core, we find a similar mismatch, i.e. a systematic underestimate of the derived $\tau_{8\ \mu\text{m}}$. Empirically, we find by applying a constant scaling factor to the derived $\tau_{8\ \mu\text{m}}$, the consistency with predicted $\tau_{8\ \mu\text{m}}$ can be achieved at the peak region and most of the extended region we are interested in (see more in Appendix D). The scaling factor for L429, L694-2 and L1517B is determined to be 2.5, 2 and 1.5, respectively.

In the final step, using these factors, we manually scaled up the $\tau_{8\ \mu\text{m}}$ map to match that of $\tau_{8\ \mu\text{m}, 850\ \mu\text{m}}^{\text{pred}}$ (or $\tau_{8\ \mu\text{m}, 250\ \mu\text{m}}^{\text{pred}}$). The scaling essentially adds back the contribution of absorption from gas structures in front of the core, related to the parental cloud where the foreground emission level is most likely to be underestimated. The obtained $N(\text{H}_2)$ maps were smoothed to $5''$ to match the NH_3 observations. The smoothed maps are shown in Fig. 1.

3.2. Core density profiles constrained from $N(\text{H}_2)$ maps

We assume that the volume density profile, $n(r)$, of the cores follow a Bonnor-Ebert like model (Dapp & Basu 2009),

$$n(r) = \frac{n_c}{(r/r_{\text{flat}})^2 + 1}. \quad (1)$$

Specifically, the radial profile has a central flat region of radius r_{flat} , i.e. a ‘‘plateau’’, plus a power-law decline $\propto r^{-2}$ at the outer radii up to the radius of the core, R . Since R is mostly degenerate with n_c , we fix R to 0.1 pc for the three cores. The corresponding functional form of column density profile is derived by integrating from the center of the core to a certain projected radius, x . We obtained the best-fit n_c and r_{flat} for the three cores, listed in Table 2. The fitted profile is shown in Fig. 2 comparing the fitted form with the measurements for the three cores separately, and in Fig. 3 for the three fitted profiles in conjunction. L429 shows the highest central density of $\sim 10^6\ \text{cm}^{-3}$. L1517B and L694-2 have similar central plateau size of ~ 3000 au, with L694-2 showing two times higher central density, of $8 \times 10^5\ \text{cm}^{-3}$. The enclosed core mass within 0.05 pc of L429 and L694-2 are $\sim 8M_\odot$ and $\sim 4M_\odot$, while that of L1517B is $\sim 2M_\odot$. In Fig. 3, it can be seen that the density profiles rise from L1517B to L429, so that the

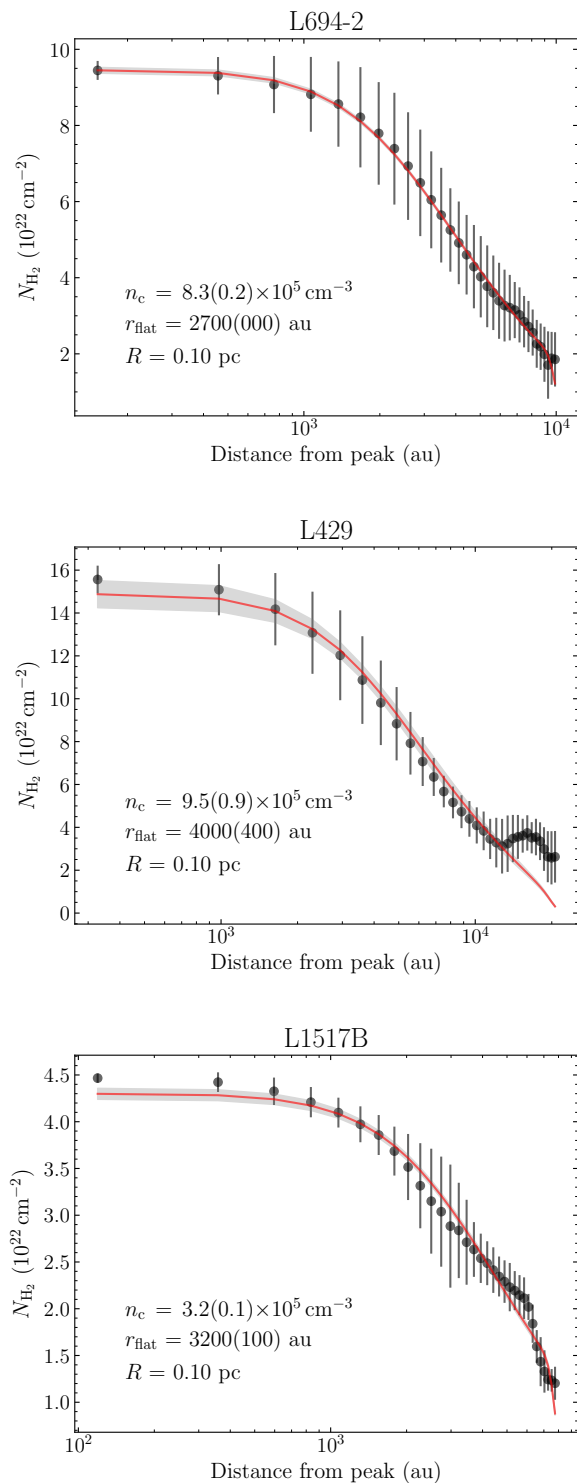


Fig. 2. The azimuthally averaged column density radial profiles, derived from the $N(\text{H}_2)$ map (Fig. 1). The solid red line shows the curve of the best-fit model following Eq. 1. The best-fit parameters of central density, n_c , and radius of inner flat region, r_{flat} , are indicated in each subplot.

density in L429 is at all radii higher than that in the other two cores.

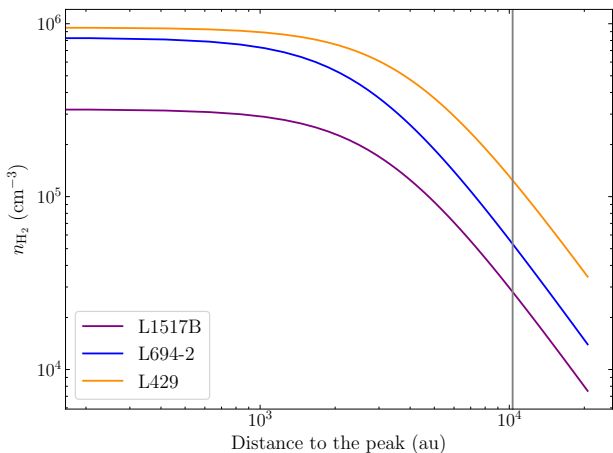


Fig. 3. The fitted density profiles of the three cores following the form of Dapp & Basu (2009). The vertical line marks a radius of 0.05 pc.

3.3. Fits of the NH_3 lines

To derive the physical parameters, we fit the NH_3 (1,1) and (2,2) lines simultaneously with functions in `pyspecnest`⁶ package (Sokolov et al. 2020). The method adopts Bayesian model selection to determine the spectral multiplicity, i.e. number of velocity components, for the observed spectrum. This has been done in the past to better fit multiple components (Chen et al. 2022, Choudhury in prep.). A nested sampling algorithm is used to explore the parameter space (`pymultinest`⁷, Buchner et al. 2014), ideal for parameter estimation in the case of multi-modal distribution. We use the `cold ammonia` model in `pyspeckit` package⁸ (Ginsburg et al. 2022) which assumes that only the (1,1) and (2,2) states of para- NH_3 are populated rotational levels, which is valid for cold cores (see Friesen et al. 2017). The fitting outputs best-fit parameters including system velocity, v_{LSR} , velocity dispersion, σ_v , kinetic temperature, T_{kin} , excitation temperature, T_{ex} , and NH_3 column density, $N(\text{NH}_3)$. The ortho-to-para NH_3 ratio is set to 1. We assume uniform priors for all the parameters with boundaries set to reflect reasonable ranges for respective source.

We note that although the total optical depth of the NH_3 (1,1) can be high in the central core area ($\tau_{1,1} \gtrsim 30$), the fact that satellite lines of (1,1) are only marginally optically thick, e.g., the two hyperfine components of $F=0-1$ at 23.6929 GHz have opacities of 0.074 and 0.15 times of $\tau_{1,1}$ and appear to be isolated components given the typical velocity dispersions associated with these cores, and that the total optical depth of the NH_3 (2,2) is $\lesssim 0.3$ ensure that the derivation of T_{kin} and $N(\text{NH}_3)$ are not biased in the physical regimes in consideration. The uncertainties and degeneracies of the parameters that come with the assumptions of the model itself, i.e., a homogeneous gas layer of constant temperature along line-of-sight, are properly estimated by the posterior probability distributions from the nested-sampling method (Sokolov et al. 2020).

Following the logic elaborated in Sokolov et al. 2020, we set the threshold of Bayes factor, $\ln K_1^2 \geq 5$, for identifying spectra that show an apparent secondary velocity component. Within

our achieved rms, it turns out that for L1517B a one-component model can describe all spectra across the core, while for L694-2 and L429, there are localised sub-regions that show evidence of two velocity components. We show the $\ln K_1^2$ maps in Appendix A. The nature of these sub-regions are discussed in Sect. 4.4. In finalising the fitted parameter maps, following Pineda et al. (2015, 2022), we trimmed the pixels with uncertainties of T_{kin} or T_{ex} larger than 1 K, or uncertainties of v_{LSR} or σ_v larger than two channel widths (0.2 km s^{-1}). These criteria also ensure that $N(\text{NH}_3)$ is well constrained, with uncertainties $\lesssim 20\%$, as reflected from the posterior probability distributions. Small, isolated regions of less than a beam size are also removed from the final maps. Since even for L694-2 and L429, the majority of the core region is characterised by one velocity component, we present the parameter maps from the one-component model for the three cores, T_{kin} and $N(\text{NH}_3)$ in Fig. 4, v_{LSR} and σ_v in Fig. 5.

3.4. NH_3 column density, kinetic and excitation temperature

Comparing the $N(\text{NH}_3)$ of the three cores in Fig. 4, the range of $N(\text{NH}_3)$ of core L429 and L694-2 is similar, reaching up to $\sim 2 \times 10^{15} \text{ cm}^{-2}$ (higher than that of H-MM1, Pineda et al. 2022), while L1517B has a lower peak $N(\text{NH}_3)$, $\sim 7 \times 10^{14} \text{ cm}^{-2}$. The morphology of the higher $N(\text{NH}_3)$ structures of L694-2 and L429 appear elongated, along the north-west to south-east, and the North to the South direction, respectively, while that of L1517B appears more roundish.

The T_{kin} spatial distribution of all three cores are mostly uniform (Fig. 4), with a slight increase towards the outer region; this is similar to T_{kin} map of H-MM1 (Pineda et al. 2022). Compared to H-MM1 that has an average central T_{kin} of 11 K, L429 and L694-2 show an overall lower T_{kin} , varying between 8-10 K. The temperature drop in the central core region is more obvious in the left plot of Fig. 6: the average temperatures of L429 drops from ~ 9 K to below 8 K, of L1517B from ~ 11 K to 10 K, while L694-2 shows a more smooth temperature structure around ~ 9 K.

Comparing T_{kin} with T_{ex} (Fig. 7), for L1517B, T_{ex} is systematically lower than T_{kin} . This indicates that the gas densities are relatively low and NH_3 lines are mainly sub-thermally excited (the thermalisation density of NH_3 (1,1) is $\sim 10^{5.5} \text{ cm}^{-3}$ for a gas kinetic temperature of ~ 10 K, Shirley 2015). For L694-2, the T_{ex} is closer to T_{kin} ; L429 shows the least overall difference between T_{ex} and T_{kin} . The comparison between T_{kin} and T_{ex} implies a progressively denser gas environment of core L1517B, L694-2 and L429, which is compatible with the density profiles determined in Sect. 3.2 (Fig. 3).

3.5. Velocity field, velocity dispersion and velocity gradient distribution

The centroid velocities of the three cores show small variations (Fig. 5), within $\sim 0.4 \text{ km s}^{-1}$. For L694-2 and L429, the variations are within $\sim 0.3 \text{ km s}^{-1}$ and for L1517B within $\sim 0.15 \text{ km s}^{-1}$. The velocities of L694-2 and L1517B are more continuous across the core dominated by mostly large-scale variations, while L429 is characterised by a more complex velocity field with localised variations, showing alternating blue- and red-shifted velocity sub-regions. For all three sources, the most red-shifted and blue-shifted velocities located at the outer regions of the core.

The velocity dispersions, σ_v , of the three cores are all below 0.2 km s^{-1} , with L1517B showing even smaller values, of $\lesssim 0.1 \text{ km s}^{-1}$. The smallest σ_v are located at the outer core re-

⁶ <https://github.com/vlas-sokolov/pyspecnest>

⁷ <https://johannesbuchner.github.io/PyMultiNest/>

⁸ <https://github.com/pyspeckit/pyspeckit>

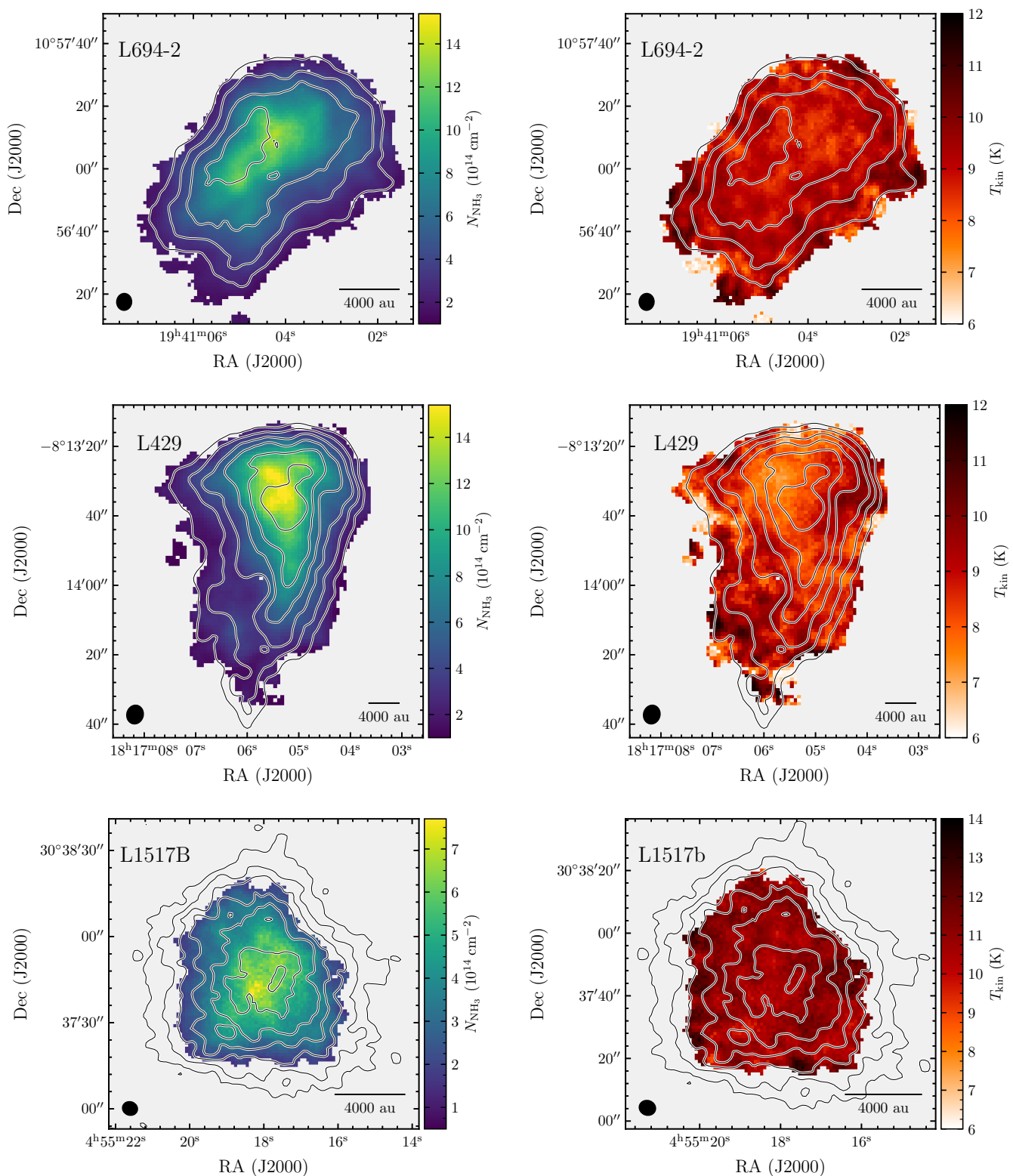


Fig. 4. The ammonia column density, $N(\text{NH}_3)$ and kinetic temperature, T_{kin} maps for the three cores, constrained from one-component fit. The beam size is indicated as a black filled circle in each image. The contours are the same as that defined in Fig. 1, showing the $N(\text{H}_2)$ levels.

gions (for L694-2 and L429 in the South-West, for L1517B in the South), coincident with continuous, either red-shifted or blue-shifted velocity field. There are some prominent, arc-like features of high σ_v seen towards L429 and L694-2, which are also correlated with abrupt change of v_{LSR} or/and appearance of sec-

ondary velocity component (Appendix F). We discuss the specific gas kinematics for each core in Sect. 4.4.

Using the centroid velocity maps, we calculated the local (line-of-sight) velocity gradient (magnitude, \mathcal{G} , and orientation, Θ) following the method elaborated in Sokolov et al. (2019), which was first presented by Goodman et al. (1993)

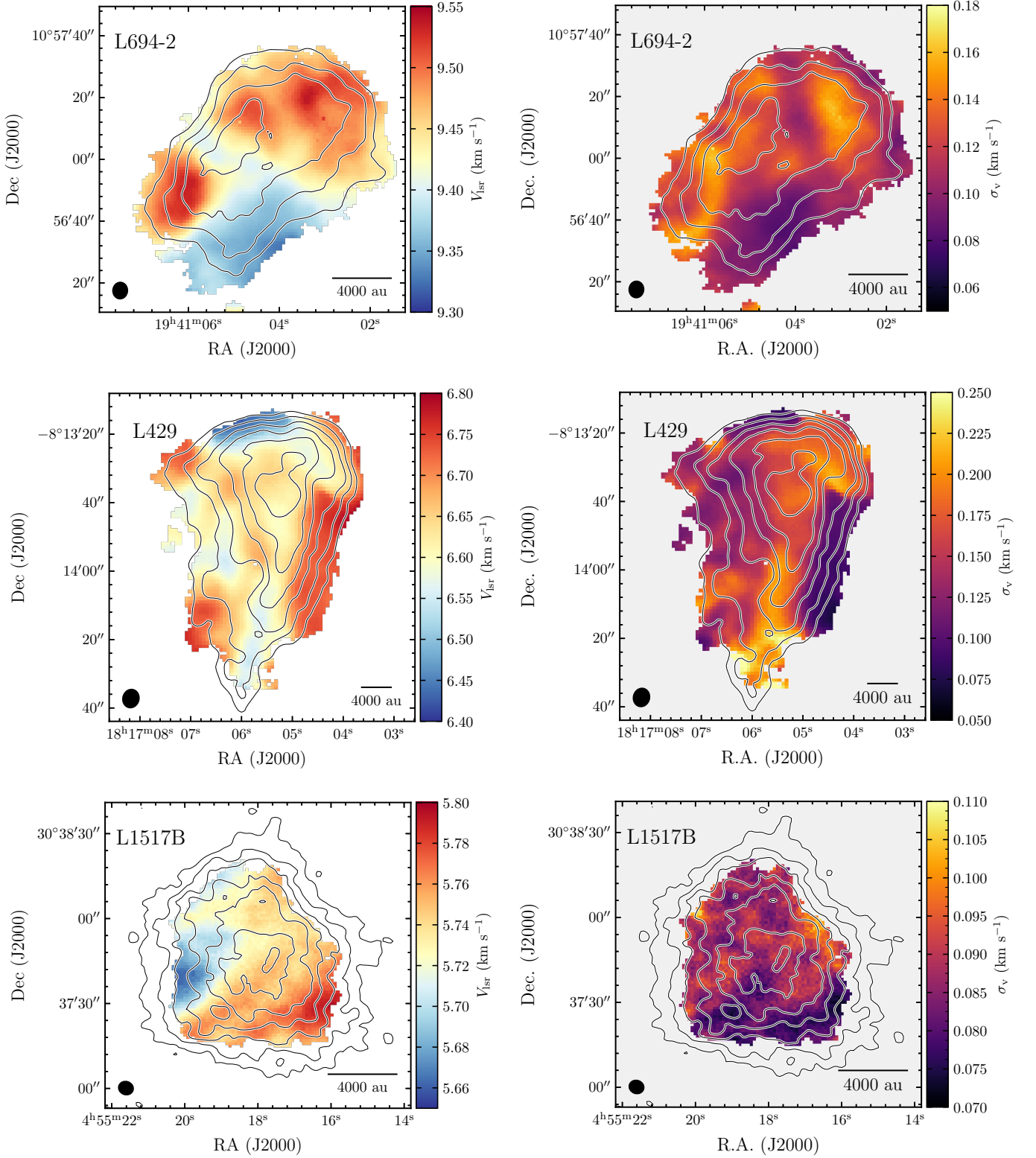


Fig. 5. The centroid velocity, v_{LSR} and velocity dispersion, σ_v maps for the three cores, constrained from one-component fit. The beam size is indicated as a black filled circle in each image.

and Caselli et al. 2002a. The chosen area for fitting the local velocity gradient and the pruning of the pixel-wise fits (based on significance of the fitted \mathcal{G} and Θ) follow that described in Sokolov et al. (2019). The sub-regions where a secondary velocity component is detected are trimmed for the

local velocity gradient calculation. We first calculate an average global velocity gradient across the core, which takes into account all the valid pixels in the centroid velocity maps. The average global velocity gradient for L694-2 is $1.65 \pm 0.03 \text{ km s}^{-1} \text{ pc}^{-1}$, for L429 is $0.52 \pm 0.02 \text{ km s}^{-1} \text{ pc}^{-1}$, and

for L1517B is $1.77 \pm 0.03 \text{ km s}^{-1} \text{ pc}^{-1}$. These small-scale velocity gradients are in general larger than those measured from the single-dish observations towards the parental filamentary structure of the cores (see for L1517B in Hacar & Tafalla (2011) and L694-2 in Kim et al. (2022)). This reflects that the small-scale structure of the core is showing more variations of velocity field.

In Fig. 8 the obtained local velocity gradient maps of the three cores are shown. The velocity gradients have a wide range of directions, which can vary significantly over small scales, especially towards L694-2 and L429. The larger magnitudes of velocity gradient are not necessarily associated with higher $N(\text{NH}_3)$ regions. In fact, towards L429 in particular, the largest \mathcal{G} mostly lie in the outer region of the core (in the North and West). Towards L694-2, despite the unpatterned overall variations of Θ , some localised regions show converging velocity gradient, e.g. in the North-west direction, which may be driven by clumpy substructures that remain unresolved.

Fig. 9 compares the distribution of \mathcal{G} : among the three cores, L429 exhibits a bi-modal distribution of \mathcal{G} , and has an average \mathcal{G} of $3.2 \pm 1.4 \text{ km s}^{-1} \text{ pc}^{-1}$, similar to that measured toward L694-2 and L1517B, of $4.7 \pm 2.6 \text{ km s}^{-1} \text{ pc}^{-1}$ and $3.5 \pm 2.1 \text{ km s}^{-1} \text{ pc}^{-1}$, respectively. If we assume that the measured line-of-sight velocity gradients partially reflect the inward motions of the dense gas, then the higher average local velocity gradients of L694-2 and the higher velocity gradients in second peak of L429 imply independently that they are denser than L1517B, having a higher enclosed mass at similar scales. The more complex velocity gradient pattern of L429 also indicates it has more chaotic gas flows, than the other two cores.

3.6. Variations of NH_3 abundance

In the left plot of Fig. 10, the comparisons between $N(\text{NH}_3)$ and $N(\text{H}_2)$ of the three cores are shown. L694-2 and L1517B do not show any strong evidence of abundance drop of NH_3 ; L429, on the other hand, show a continuous flattening of $N(\text{NH}_3)$ as $N(\text{H}_2)$ increases. In order to account for different background levels of H_2 column density, we estimate the average $N(\text{H}_2)$ offset, $N_{\text{H}_2, \text{off}}$, from the outermost region (~ 3 beam sizes in width) of the $N(\text{NH}_3)$ map (“zero-level” of $N(\text{NH}_3)$, see also below), and plot the $N(\text{NH}_3)$ as a function of $N(\text{H}_2) - N_{\text{H}_2, \text{off}}$ in Fig. 10, right panel. It can be seen that the slopes of L429 and L694-2 are similar in the lower $N(\text{H}_2) - N_{\text{H}_2, \text{off}}$ regime of up to $\sim 5 \times 10^{22} \text{ cm}^{-3}$, with L1517B showing a higher abundance of NH_3 ; the positive offsets of NH_3 at $N(\text{H}_2) = N_{\text{H}_2, \text{off}}$ are similar among the three cores of $\sim 2 \times 10^{14} \text{ cm}^{-2}$, indicating similar NH_3 column density in their embedding molecular clouds.

To describe the variation of $N(\text{NH}_3)$ as a function of $N(\text{H}_2)$, we fit a broken line model following the form detailed in Pineda et al. (2022). The functional form includes two linear slopes a and c , which apply at below and above the cutoff $N(\text{H}_2)$, x_0 , where the variation happens, in addition to an intercept b representing the $N(\text{NH}_3)$ at $N(\text{H}_2) = 0$. In the case of L1517B and L694-2, the best-fit cutoff $N(\text{H}_2)$ are above the maximum $N(\text{H}_2)$ measured, indicating they are better described by a single linear relation. The fitted parameters are listed in Table 3 for the three cores: in the case of L1517B and L694-2, the best-fit cutoff $N(\text{H}_2)$ are close to the maximum $N(\text{H}_2)$ measured, indicating they are better described by a single linear relation. Compared to the case of H-MM1, values of a are similar. The cutoff $N(\text{H}_2)$ value in L429 is $\sim 8 \times 10^{22} \text{ cm}^{-2}$, which is higher than that in H-MM1. Concerning the variations of the abundance, H-MM1 shows a negative slope c at higher $N(\text{H}_2)$ which strongly indicates ammonia depletion, towards L429 we have a more flat-

tened but still positive slope c , indicating that there is only moderate ammonia depletion happening in the center.

4. Discussion

4.1. Temperature structure

We resolve a slight decrease of gas temperature towards L429 and L1517B, varying from $\sim 9 \text{ K}$ to below 8 K for L429, and $\sim 11 \text{ K}$ to 10 K for L1517B. The situation resembles the case of H-MM1 (Pineda et al. 2022), while H-MM1 shows an overall higher temperature, ranging from $\sim 12 \text{ K}$ to 11 K . L694-2 shows a rather uniform temperature around 9 K , which is consistent with previous findings that suggest it is a prolate core slightly inclined to the line-of-sight (Harvey et al. 2003). Compared to L1544 that displays a strong temperature drop down to $\sim 6 \text{ K}$ (Crapsi et al. 2007), these temperature variations are minor. Previous single-dish observations of NH_3 towards starless core L1517B report a constant temperature of 9.5 K (Tafalla et al. 2002, 2006), while with our improved angular resolution, we still only resolve a minor decrease of temperature, which is similar to that resolved in starless core CB17 (Spear et al. 2021) and the northern Ophiuchus D core (Ruuskanen et al. 2011). The nearly isothermal nature of these cores suggests that they are at an earlier stage of evolution (Keto & Caselli 2008b), characterised by a low gas density $\lesssim 10^5 \text{ cm}^{-3}$ (line-of-sight averaged density seen by NH_3) and cooling for the bulk gas is governed by molecular line emission.

The temperature drop in our sampled three cores is less significant than that in the prototypical pre-stellar core L1544, which is likely at a more evolved stage of evolution. In L1544, there is a drastic temperature drop seen in the inner $\sim 2500 \text{ au}$ down to 6 K (Crapsi et al. 2007), while L429 has a similar central density and evolutionary stage as L1544, the fact that it locates further away with an achieved angular resolution similar to 2500 au may also have hindered the significant temperature drop to be probed. One note is that Crapsi et al. (2007) used VLA-only data to estimate T_{kin} ; in Appendix E we present the variations of T_{kin} derived from VLA-only data cubes, Crapsi et al. (2007), which also only show minor drop of temperature.

4.2. Characterising the temperature structure of the cores: radiative transfer modeling with RADMC-3D

The central drop of gas and dust temperature in pre-stellar cores is due to shielding and irradiation of their embedded radiation field. We note that the derivation of a temperature map assuming homogeneous layer(s) is subject to line-of-sight averaging effect and cannot fully recover the possible underlying temperature gradient. A full radiative transfer (RT) modeling incorporating the density, temperature and NH_3 abundance profiles tailored for the sampled cores may be more sensitive to the subtle change of the temperature structure, which is beyond the scope of this work. To understand the environment interstellar radiation field of the three cores and to gauge the gas temperature variations from NH_3 lines, we conducted radiative transfer modelling with RADMC-3D (Dullemond et al. 2012), assuming that the density structure of the cores follows the 1-dimensional form derived in Sect. 3.2. We start the modeling by assuming a standard interstellar radiation field (ISRF) following the form in Hocuk et al. (2017), which consists of six modified black body components (Zucconi et al. 2001) and a UV contribution (Draine 1978). We adjust the scaling of the standard ISRF and arrive at different dust temperature profiles. The mass averaged temperature

Table 3. Best-fit parameters of the broken line model of the three cores and H-MM1 (Pineda et al. 2022)

Parameter	L694-2*	L429	L1517B*	H-MM1	Unit
a	1.3(0.4)	1.3(1.1)	1.6(0.6)	2.0	$\times 10^{-8}$
b	-0.5(6.0)	-1.6(4.6)	-1.0(3.3)	1.1	$\times 10^{14} \text{ cm}^{-2}$
c	-	0.73(6.6)	-	-1.1	$\times 10^{-8}$
x_0	-	7.5(2.0)	-	2.6	$\times 10^{22} \text{ cm}^{-2}$

* A linear relation is fitted to L1517B and L694-2 instead of the broken line model.

Uncertainty of the parameter is listed in brackets, in percentage unit with respect to the best-fit value.

profile is then calculated, assuming the threshold above which the gas structures are seen by NH_3 emission are $1 \times 10^4 \text{ cm}^{-3}$ for L1517B, and $2 \times 10^4 \text{ cm}^{-3}$ for L429 and L694-2. The thresholds are determined by comparing the observed T_{ex} and T_{kin} relation for each source to the modelled T_{ex} vs. T_{kin} relation based on non-LTE calculations for NH_3 column density of $6 \times 10^{14} \text{ cm}^{-2}$ (Shirley 2015).

In Fig. 11 we plot the output radial temperature profiles from RADMC-3D, together with the (projected) radial profile after mass averaging along LOS considering the density profile constrained in Sect. 3.2. The observed physical resolution is also taken into account in the mass averaging. If we assume that dust and gas are fully coupled above a gas density of 10^5 cm^{-3} (Goldsmith 2001, indicated by the vertical solid line in Fig. 11), then the resultant temperature profile of $G_0 = 1-2$ for L429 matches well to the observed gas kinetic temperature derived from NH_3 , showing a slight decrease from above 9 K to 8 K within the effective radius of the T_{kin} map derived from NH_3 , while for L694-2, the $G_0 = 0.5$ ISRF produces a rather invariant ~ 9 K profile within the effective radius. Meanwhile, the NH_3 abundance drop in the central region of L429 can bring down further the mass averaged temperature to below 8 K, since there is non-uniform sampling of gas mass along LOS. For L1517B, the $G_0 = 1$ ISRF produces a temperature around 11 K, although the drop is even more slight than what is observed. We therefore conclude that considering the high central density of the three cores, the gas kinetic temperatures seen by NH_3 are consistent with the dust temperatures assuming the cores are bathed in standard ISRF ($G_0 \sim 1-2$). A more significant radial temperature variation towards the three cores may be resolved with a higher sensitivity NH_3 mapping, i.e. to increase the effective radius of the T_{kin} map.

4.3. Abundance variations of NH_3 in pre-stellar cores

At the lower $N(\text{H}_2)$ end ($N(\text{H}_2) < 8 \times 10^{22} \text{ cm}^{-2}$), the abundance of NH_3 of the three cores are close, as indicated by their similar slopes between $N(\text{NH}_3)$ and $N(\text{H}_2)$ (Table 3), $\sim 1.5 \times 10^{-8}$. This abundance value is close to previous interferometric measurements towards other pre-stellar cores (Chitsazzadeh et al. 2014, Spear et al. 2021, Friesen et al. 2017, Pineda et al. 2022) within a factor of 2.

Adopting the new distance measurements of the three cores (Galli et al. 2019, Kim et al. 2022, Ortiz-León et al. 2018), with the high-resolution extinction map, we derive the central densities of the three cores increase from L1517B to L429; L1517B has a central density of $\sim 3 \times 10^5 \text{ cm}^{-3}$, ~ 3 times lower than that towards L694-2 and L429. The fact that NH_3 abundances of L694-2 and L1517B do not vary as significantly as L429 in the

core center is likely due to their overall lower density. From the relation of $N(\text{NH}_3)$ and $N(\text{H}_2)$ (Fig. 10) of L429, the cutoff $N(\text{H}_2)$ where the abundance drops is fitted to be $\sim 7.5 \times 10^{22} \text{ cm}^{-3}$, and the abundance in the core center is 2 times lower than at core edge (comparing a and c in Table 3). This abundance variations are similar to L1689-SMM16 (Spear et al. 2021). As we use a 1-D model to describe the core density profile, we can convert the cutoff $N(\text{H}_2)$ to LOS mass averaged gas volume density ($\langle N(\text{H}_2) \rangle$), yielding $4.4 \times 10^4 \text{ cm}^{-3}$ for L429. Pineda et al. 2022 suggests a turnover gas density of $2.1 \times 10^5 \text{ cm}^{-3}$, beyond which the NH_3 depletion is significant. With the conversion of $N(\text{H}_2)$ to $\langle N(\text{H}_2) \rangle$, none of the three cores has $\langle N(\text{H}_2) \rangle$ reaching $2.1 \times 10^5 \text{ cm}^{-3}$ with the present angular resolution. This explains the moderate NH_3 depletion towards L429, compared to that resolved in H-MM1, as well as the rather invariant NH_3 abundance towards L694-2 and L1517B, which are due to their progressively lower gas densities compared to L429. This observational trend of NH_3 abundance variations is consistent with predictions of chemical models that show various degree of NH_3 depletion in the central region of the cores (Sipilä et al. 2019).

Embedded in different parental molecular clouds (see Appendix A), the three cores and H-MM1 have different environmental conditions, which are also reflective in their different average temperature (dominated by the outer parts of the core), and different levels of $N(\text{H}_2)$ offset (Sect. 3.6). The fact that the NH_3 abundance variation of the four cores can be consistently explained by their different central densities seems to suggest that the only relevant physical property for the depletion of NH_3 is the evolutionary stage of the core.

4.4. Gas kinematics

As described in Sect. 3.5, the velocity dispersions, σ_v for the three cores show local variations, but are all $\lesssim 0.2 \text{ km s}^{-1}$. We can estimate the thermal and non-thermal contributions using the derived T_{kin} , while taking into account the instrumental broadening due to the channel-to-channel correlation (Pineda et al. 2010, Leroy et al. 2016, Choudhury et al. 2020). The distribution of the sonic Mach number, M_s , of the three cores is shown in Fig. 12. The cores all appear predominantly subsonic ($M_s \leq 1$): L1517B shows the least non-thermal contribution with an average M_s of 0.2; L694-2 is intermediate with an average M_s of 0.5, and L429 shows the highest M_s , on average of 0.8. The highest M_s towards L429 is consistent with its more complex velocity field and higher velocity gradient.

Considering the stability of the cores, we can compare the scale of the inner plateau a with the Jeans length estimated from central density n_c and temperature; the scale ratio is denoted as k

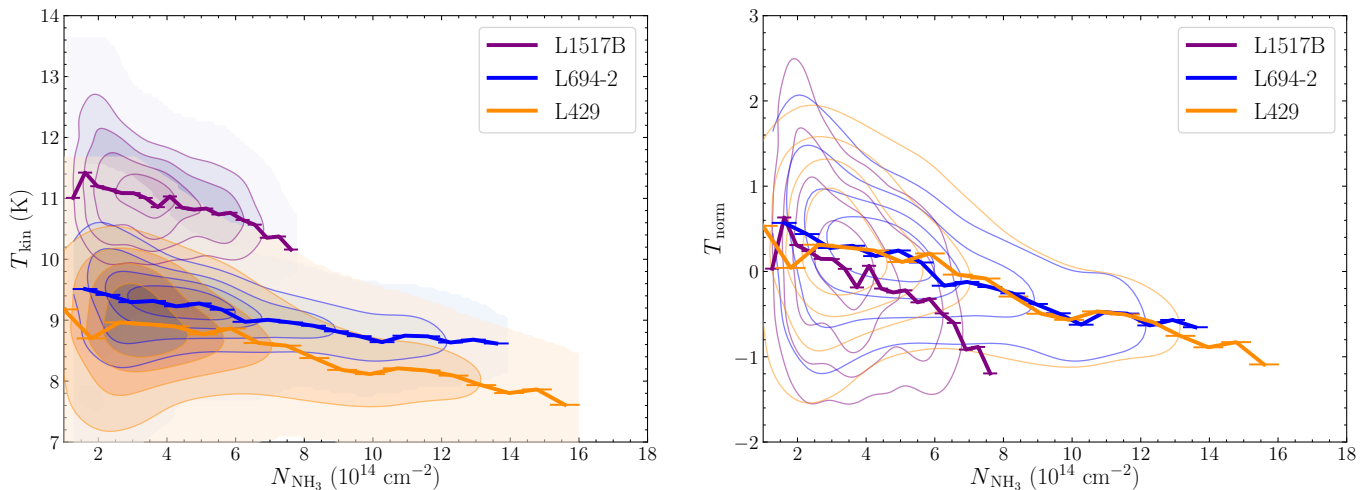


Fig. 6. KDE of kinetic temperature (*left*) and normalised kinetic temperature (*right*) as a function of NH_3 column density. In the *right* figure, the kinetic temperatures of each source are transformed with $T_{\text{norm}} = T_{\text{kin}} - T_{\text{kin}}^- / \sigma_{T_{\text{kin}}}$.

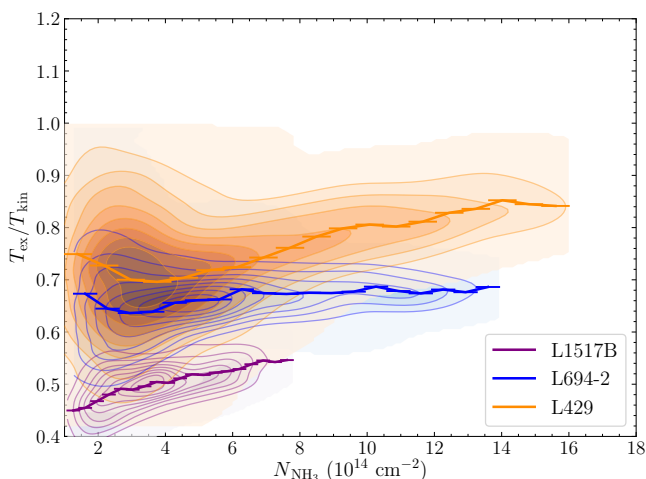


Fig. 7. The Gaussian KDE of the ratio of $T_{\text{ex}}/T_{\text{kin}}$ as a function of NH_3 column density. The line segments correspond to mean values in NH_3 column density bins, with solid lines linked together.

in Dapp & Basu 2009. For similar gas density and temperature, the larger a corresponds to a reduced pressure gradient, and the core is more likely collapsing with prevailing self-gravity. With central temperatures of 10 K of L1517B and 8 K for L694-2 and L429, we arrive at k values of 0.8 of L1517B and 1.3 for both L694-2 and L429. Since the central temperature is estimated from the T_{kin} maps, which involve LOS averaging, which for a centrally dropping temperature profile, is higher than the real temperature, these k values are likely upper limits. Nonetheless, this suggests that L429 and L694-2 are in a more evolved evolutionary phase than L1517B.

The embedding filament of L1517B shows signatures of velocity oscillation (Hacar & Tafalla 2011) and the core itself seems to reside at the position of converging velocities. The parental filamentary structure exhibits a similar velocity field among tracers sensitive to different density regimes (Hacar &

Tafalla 2011), appearing to be a velocity coherent structure up to 0.5 pc with subsonic motions. Indeed, the resolved continuous variation of the velocity field inside L1517B, from north-east to south-west (Fig. 5), roughly follows the large-scale filament structure where the velocity gradients may vary in direction due to the flow converging. The velocity turning from the large-scale filament may also originate partially from the filament rotation (e.g., Álvarez-Gutiérrez et al. 2021). This may reflect that the physical status of L1517B is close to quasi-static contraction, with the small-scale velocity gradient ($\sim 2 \text{ km s}^{-1} \text{ pc}^{-1}$, Sec. 3.5) slightly larger than that along the embedding filament ($\sim 1.4 \text{ km s}^{-1} \text{ pc}^{-1}$).

For L694-2 and L429, the sharp gradients and multiple velocity components (in sub-regions, Appendix F) found at the edge of the cores might be the signature of the ongoing accretion of material from cloud to core (e.g., Choudhury et al. 2020, 2021, Chen et al. 2022), which remains to be further studied with larger-scale maps and with better sensitivity. Cloud to core accretion has already been deduced with observations of HCO^+ (e.g. Redaelli et al. 2022) and CS (e.g. Mardones et al. 1997). How these cloud-core feeding flows link to the even smaller scale asymmetric accretion streamers surrounding the young stellar objects (core to disk flows, e.g., Pineda et al. 2020, 2023) carry essential clues of how protostars gain masses under the complex interplay of physical mechanisms over different spatial scales.

5. Conclusions

We present $\text{NH}_3(1,1)$ and $(2,2)$ data combined from VLA and GBT observations, for one starless core L1517B, and two pre-stellar cores L694-2 and L429. We derive the parameter maps from fitting the NH_3 lines and obtain the gas kinetic and excitation temperature, NH_3 column density, centroid velocity and velocity dispersion maps. We use *Spitzer* $8 \mu\text{m}$ to derive high angular resolution hydrogen column density maps for the three cores. Our main findings are as follows.

- A minor temperature drop is resolved towards L429 and L1517B, showing $\sim 9 \text{ K}$ at core edge to below 8 K in center, and $\sim 11 \text{ K}$ to 10 K, respectively. L694-2 shows a uniform

temperature structure, of ~ 9 K. These resolved gas radial temperature profiles are roughly consistent with each core's LOS mass averaged dust temperature profiles with a standard ISRF, considering their different gas density profiles and our effective mapping scales.

- The Bonnor-Ebert like gas density profiles are constrained from the high-resolution extinction map ($6''$). The central density of L429 and L694-2 appears the largest, $0.8\text{--}1 \times 10^6 \text{ cm}^{-3}$, while L1517B has a central density of $3.2 \times 10^5 \text{ cm}^{-3}$.
- The line-widths are predominantly subsonic with progressively overall increase from L1517B, L694-2 and L429, consistent with the increasing magnitude of the local velocity gradient. The velocity fields of L1517B and L694-2 show relatively large-scale variations, likely reflecting a mixture of contracting motions and acoustic oscillation. L429 exhibits more localised velocity changes, possibly reflecting an advanced collapse phase that involves more complex gas motions.
- The NH_3 abundance becomes ~ 2 times lower in the central region of L429, which happens around hydrogen column density of $7.5 \times 10^{22} \text{ cm}^{-2}$. The corresponding H_2 volume density is $4.4 \times 10^4 \text{ cm}^{-3}$. This is below the cutoff density of $\sim 2 \times 10^5 \text{ cm}^{-3}$ where a stronger abundance drop is seen towards H-MM1 (Pineda et al. 2022). L694-2 and L1517 show a rather invariant NH_3 abundance. Overall, the three cores plus H-MM1 compose a consistent trend of NH_3 depletion with increasing gas density in the central region of pre-stellar cores.

Acknowledgements. The authors acknowledge the financial support of the Max Planck Society. H.B.L. is supported by the National Science and Technology Council (NSTC) of Taiwan (Grant Nos. 111-2112-M-110-022-MY3).

References

- Aikawa, Y., Herbst, E., Roberts, H., & Caselli, P. 2005, *ApJ*, 620, 330
- Álvarez-Gutiérrez, R. H., Stutz, A. M., Law, C. Y., et al. 2021, *ApJ*, 908, 86
- Bacmann, A., Lefloch, B., Ceccarelli, C., et al. 2003, *ApJ*, 585, L55
- Bergin, E. A., Maret, S., van der Tak, F. F. S., et al. 2006, *ApJ*, 645, 369
- Bergin, E. A. & Tafalla, M. 2007, *ARA&A*, 45, 339
- Buchner, J., Georgakakis, A., Nandra, K., et al. 2014, *A&A*, 564, A125
- Butler, M. J. & Tan, J. C. 2009, *ApJ*, 696, 484
- Caselli, P. & Ceccarelli, C. 2012, *A&A Rev.*, 20, 56
- Caselli, P., Pineda, J. E., Sipilä, O., et al. 2022, *ApJ*, 929, 13
- Caselli, P., Pineda, J. E., Zhao, B., et al. 2019, *ApJ*, 874, 89
- Caselli, P., Vastel, C., Ceccarelli, C., et al. 2008, *A&A*, 492, 703
- Caselli, P., Walmsley, C. M., Tafalla, M., Dore, L., & Myers, P. C. 1999, *ApJ*, 523, L165
- Caselli, P., Walmsley, C. M., Zucconi, A., et al. 2002a, *ApJ*, 565, 331
- Caselli, P., Walmsley, C. M., Zucconi, A., et al. 2002b, *ApJ*, 565, 344
- Chacón-Tanarro, A., Caselli, P., Bizzocchi, L., et al. 2017, *A&A*, 606, A142
- Chacón-Tanarro, A., Pineda, J. E., Caselli, P., et al. 2019, *A&A*, 623, A118
- Chapin, E. L., Berry, D. S., Gibb, A. G., et al. 2013, *MNRAS*, 430, 2545
- Chen, M. C.-Y., Di Francesco, J., Pineda, J. E., Offner, S. S. R., & Friesen, R. K. 2022, *ApJ*, 935, 57
- Chitsazadeh, S., Di Francesco, J., Schnee, S., et al. 2014, *ApJ*, 790, 129
- Choudhury, S., Pineda, J. E., Caselli, P., et al. 2020, *A&A*, 640, L6
- Choudhury, S., Pineda, J. E., Caselli, P., et al. 2021, *A&A*, 648, A114
- Crapsi, A., Caselli, P., Walmsley, C. M., et al. 2005, *ApJ*, 619, 379
- Crapsi, A., Caselli, P., Walmsley, M. C., & Tafalla, M. 2007, *A&A*, 470, 221
- Currie, M. J., Berry, D. S., Jenness, T., et al. 2014, in *Astronomical Society of the Pacific Conference Series*, Vol. 485, *Astronomical Data Analysis Software and Systems XXIII*, ed. N. Manset & P. Forshay, 391
- Dapp, W. B. & Basu, S. 2009, *MNRAS*, 395, 1092
- Draine, B. T. 1978, *ApJS*, 36, 595
- Dullemond, C. P., Juhasz, A., Pohl, A., et al. 2012, *RADMC-3D: A multi-purpose radiative transfer tool*, *Astrophysics Source Code Library*, record ascl:1202.015
- Elias, J. H. 1978, *ApJ*, 224, 857
- Evans, Neal J., I., Rawlings, J. M. C., Shirley, Y. L., & Mundy, L. G. 2001, *ApJ*, 557, 193
- Flower, D. R., Pineau Des Forêts, G., & Walmsley, C. M. 2006, *A&A*, 456, 215
- Friesen, R. K., Di Francesco, J., Shirley, Y. L., & Myers, P. C. 2009, *ApJ*, 697, 1457
- Friesen, R. K., Pineda, J. E., co-PIs, et al. 2017, *ApJ*, 843, 63
- Fu, T.-M., Gao, Y., & Lou, Y.-Q. 2011, *ApJ*, 741, 113
- Galli, D., Walmsley, M., & Gonçalves, J. 2002, *A&A*, 394, 275
- Galli, P. A. B., Loinard, L., Bouy, H., et al. 2019, *A&A*, 630, A137
- Ginsburg, A., Sokolov, V., de Val-Borro, M., et al. 2022, *AJ*, 163, 291
- Goldsmith, P. F. 2001, *ApJ*, 557, 736
- Goodman, A. A., Benson, P. J., Fuller, G. A., & Myers, P. C. 1993, *ApJ*, 406, 528
- Griffin, M. J., Abergel, A., Abreu, A., et al. 2010, *A&A*, 518, L3
- Hacar, A. & Tafalla, M. 2011, *A&A*, 533, A34
- Harju, J., Daniel, F., Sipilä, O., et al. 2017, *A&A*, 600, A61
- Harju, J., Pineda, J. E., Vasyunin, A. I., et al. 2020, *ApJ*, 895, 101
- Harvey, D. W. A., Wilner, D. J., Lada, C. J., Myers, P. C., & Alves, J. F. 2003, *ApJ*, 598, 1112
- Ho, P. T. P. & Townes, C. H. 1983, *ARA&A*, 21, 239
- Hocuk, S., Szűcs, L., Caselli, P., et al. 2017, *A&A*, 604, A58
- Hotzel, S., Harju, J., Lemke, D., Mattila, K., & Walmsley, C. M. 2001, *A&A*, 372, 302
- Jiao, S., Lin, Y., Shui, X., et al. 2022, *Science China Physics, Mechanics, and Astronomy*, 65, 299511
- Juvela, M., Harju, J., Ysard, N., & Lunttila, T. 2012, *A&A*, 538, A133
- Keown, J., Schnee, S., Bourke, T. L., et al. 2016, *ApJ*, 833, 97
- Keto, E. & Caselli, P. 2008a, *ApJ*, 683, 238
- Keto, E. & Caselli, P. 2008b, *ApJ*, 683, 238
- Keto, E. & Caselli, P. 2010, *MNRAS*, 402, 1625
- Keto, E., Caselli, P., & Rawlings, J. 2015, *MNRAS*, 446, 3731
- Keto, E. & Field, G. 2005, *ApJ*, 635, 1151
- Kim, S., Lee, C. W., Tafalla, M., et al. 2022, arXiv e-prints, arXiv:2209.14943
- Kirk, J. M., Ward-Thompson, D., & Crutcher, R. M. 2006, *MNRAS*, 369, 1445
- Koumpia, E., Evans, L., Di Francesco, J., van der Tak, F. F. S., & Oudmaijer, R. D. 2020, *A&A*, 643, A61
- Lee, C. W. & Myers, P. C. 2011, *ApJ*, 734, 60
- Lee, C. W., Myers, P. C., & Plume, R. 2004, *ApJS*, 153, 523
- Lefèvre, C., Pagani, L., Min, M., Poteet, C., & Whittet, D. 2016, *A&A*, 585, L4
- Leroy, A. K., Hughes, A., Schrupa, A., et al. 2016, *ApJ*, 831, 16
- Lin, Y., Wyrowski, F., Liu, H. B., et al. 2022, *A&A*, 658, A128
- Liu, H. B., Galván-Madrid, R., Jiménez-Serra, I., et al. 2015, *ApJ*, 804, 37
- Lou, Y.-Q. & Gao, Y. 2011, *MNRAS*, 412, 1755
- Lucy, L. B. 1974, *AJ*, 79, 745
- Mardones, D., Myers, P. C., Tafalla, M., et al. 1997, *ApJ*, 489, 719
- Maret, S., Bergin, E. A., & Tafalla, M. 2013, *A&A*, 559, A53
- Monsch, K., Pineda, J. E., Liu, H. B., et al. 2018, *ApJ*, 861, 77
- Myers, P. C. & Benson, P. J. 1983, *ApJ*, 266, 309
- Ortiz-León, G. N., Loinard, L., Dzib, S. A., et al. 2018, *ApJ*, 869, L33
- Ossenkopf, V. & Henning, T. 1994, *A&A*, 291, 943
- Pagani, L., Bacmann, A., Cabrit, S., & Vastel, C. 2007, *A&A*, 467, 179
- Pineda, J. E., Arzoumanian, D., Andre, P., et al. 2023, 534, 233
- Pineda, J. E., Goodman, A. A., Arce, H. G., et al. 2010, *ApJ*, 712, L116
- Pineda, J. E., Goodman, A. A., Arce, H. G., et al. 2011, *ApJ*, 739, L2
- Pineda, J. E., Harju, J., Caselli, P., et al. 2022, *AJ*, 163, 294
- Pineda, J. E., Offner, S. S. R., Parker, R. J., et al. 2015, *Nature*, 518, 213
- Pineda, J. E., Segura-Cox, D., Caselli, P., et al. 2020, *Nature Astronomy*, 4, 1158
- Redaelli, E., Chacón-Tanarro, A., Caselli, P., et al. 2022, *ApJ*, 941, 168
- Rodgers, S. D. & Charnley, S. B. 2001, *ApJ*, 553, 613
- Roueff, E., Lis, D. C., van der Tak, F. F. S., Gerin, M., & Goldsmith, P. F. 2005, *A&A*, 438, 585
- Ruoskanen, J., Harju, J., Juvela, M., et al. 2011, *A&A*, 534, A122
- Sault, R. J., Teuben, P. J., & Wright, M. C. H. 1995, in *Astronomical Society of the Pacific Conference Series*, Vol. 77, *Astronomical Data Analysis Software and Systems IV*, ed. R. A. Shaw, H. E. Payne, & J. J. E. Hayes, 433
- Schnee, S., Brunetti, N., Di Francesco, J., et al. 2013, *ApJ*, 777, 121
- Shirley, Y. L. 2015, *PASP*, 127, 299
- Sipilä, O., Caselli, P., Redaelli, E., Juvela, M., & Bizzocchi, L. 2019, *MNRAS*, 487, 1269
- Sipilä, O., Harju, J., Caselli, P., & Schlemmer, S. 2015, *A&A*, 581, A122
- Sohn, J., Lee, C. W., Park, Y.-S., et al. 2007, *ApJ*, 664, 928
- Sokolov, V., Pineda, J. E., Buchner, J., & Caselli, P. 2020, *ApJ*, 892, L32
- Sokolov, V., Wang, K., Pineda, J. E., et al. 2019, *ApJ*, 872, 30
- Spear, S., Maureira, M. J., Arce, H. G., et al. 2021, *ApJ*, 923, 231
- Spezzano, S., Bizzocchi, L., Caselli, P., Harju, J., & Brünken, S. 2016, *A&A*, 592, L11
- Steinacker, J., Bacmann, A., Henning, T., Klessen, R., & Stickel, M. 2005, *A&A*, 434, 167
- Stutz, A. M., Bourke, T. L., Rieke, G. H., et al. 2009, *ApJ*, 690, L35
- Tafalla, M., Myers, P. C., Caselli, P., & Walmsley, C. M. 2004, *A&A*, 416, 191
- Tafalla, M., Myers, P. C., Caselli, P., Walmsley, C. M., & Comito, C. 2002, *ApJ*, 569, 815
- Tafalla, M., Santiago-García, J., Myers, P. C., et al. 2006, *A&A*, 455, 577
- Walmsley, C. M. & Ungerechts, H. 1983, *A&A*, 122, 164
- Williams, J. P., Lee, C. W., & Myers, P. C. 2006, *ApJ*, 636, 952
- Zucconi, A., Walmsley, C. M., & Galli, D. 2001, *A&A*, 376, 650

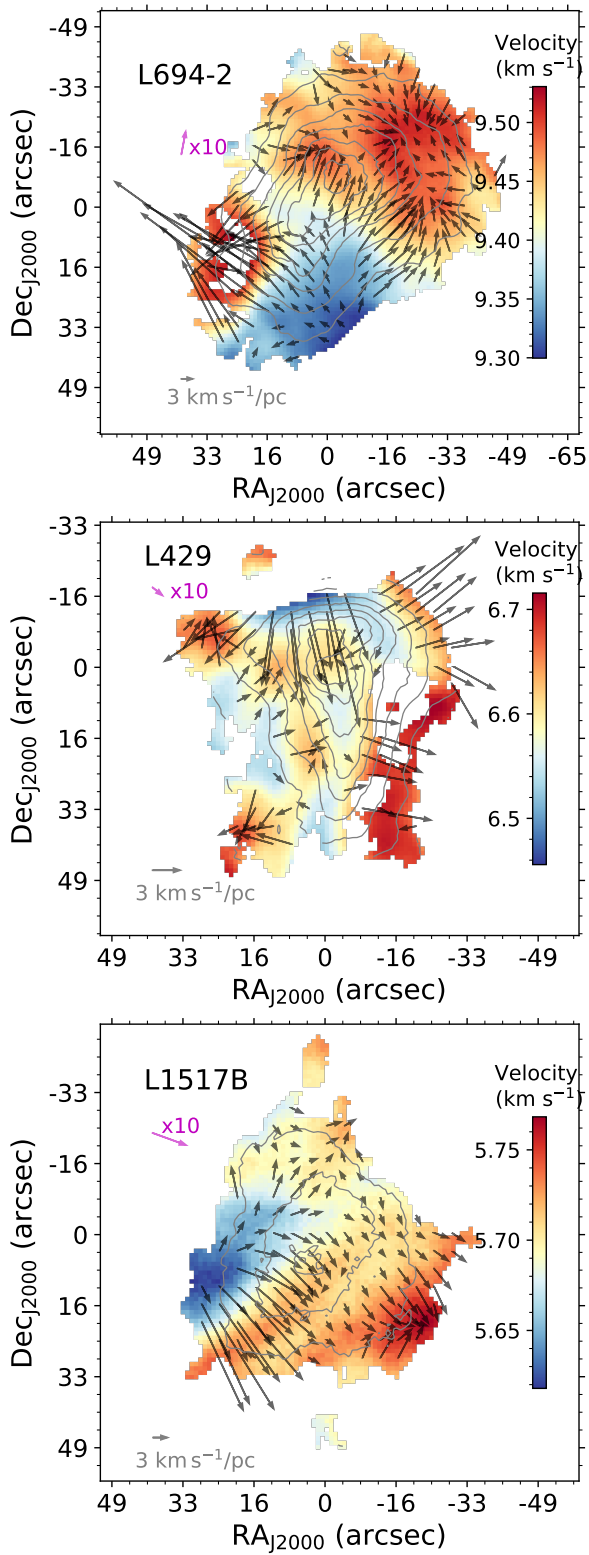


Fig. 8. Centroid velocity map overlaid with the velocity gradient (after subtracting the average overall velocity gradient) arrows. The subregions where a second velocity component is seen are excluded from the maps. The directions of the arrows points to the steepest velocity field change in the red-shifted direction, while the arrow lengths represent the relative vector magnitudes of the gradient, with the length of $3 \text{ km s}^{-1} \text{ pc}^{-1}$ indicated in each subplot. The magenta arrow shows the average overall velocity gradient across the core; the length is artificially scaled up by a factor of ten for better representation. The contour levels indicate $N(\text{NH}_3)$ starting from $1.0 \times 10^{14} \text{ cm}^{-2}$ with an interval of $2.1 \times 10^{14} \text{ cm}^{-2}$.

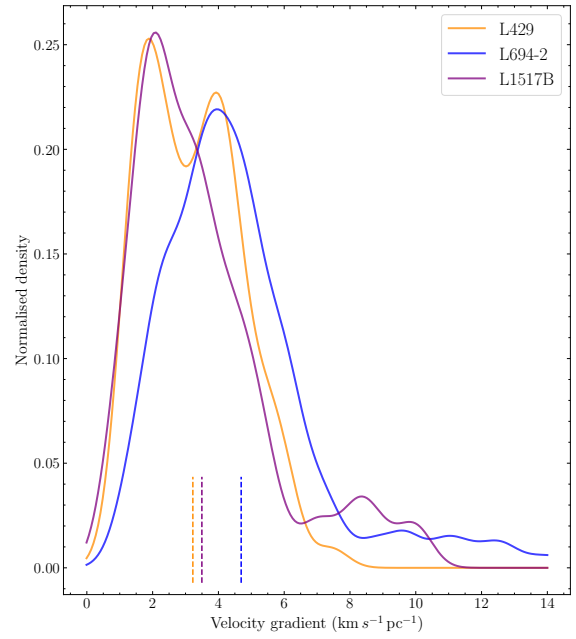


Fig. 9. Distribution of velocity gradient of the three cores.

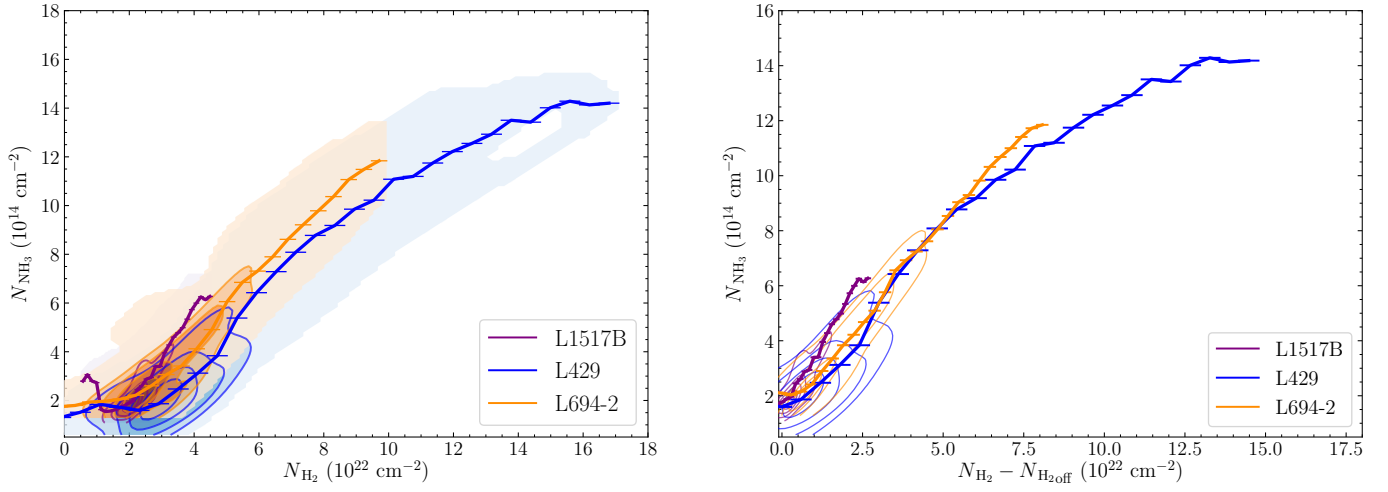


Fig. 10. The KDE of NH_3 column density as a function of H_2 column density. The line segments correspond to mean values in H_2 or NH_3 column density bins, which are linked together. In the *right* panel, H_2 column density is corrected by H_2 offset estimated based on “zero-level” of NH_3 column density.

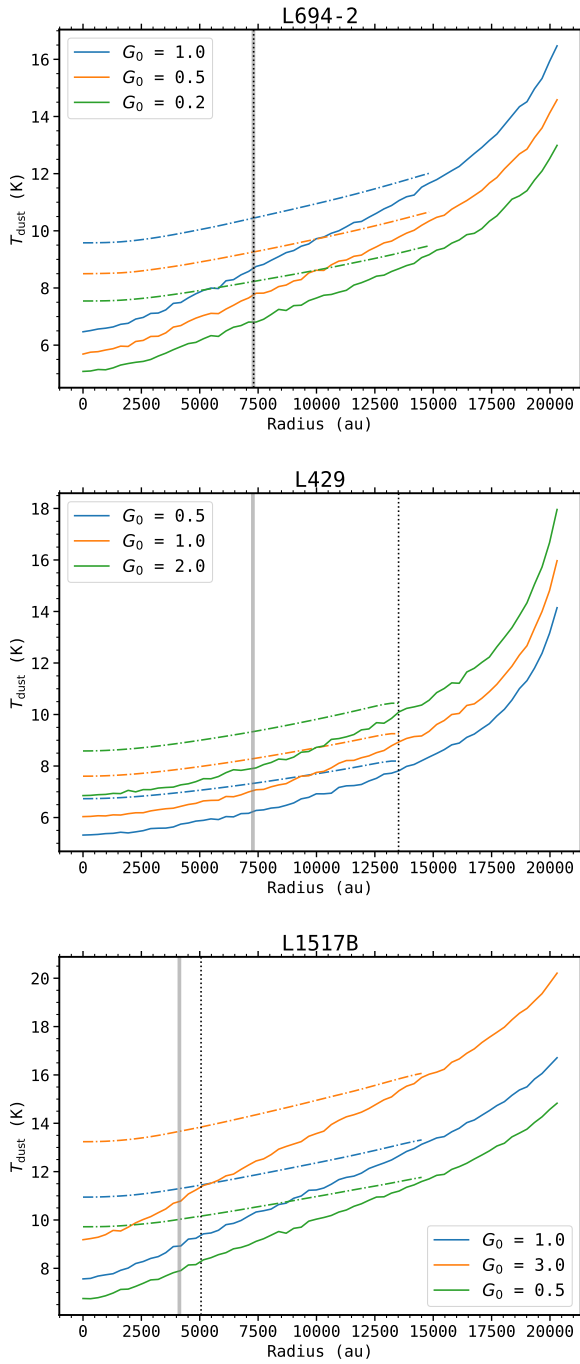


Fig. 11. Radial temperature profiles (solid lines) calculated by RADMC-3D assuming different ISRF intensity, and the correspondent LOS mass averaged temperature profiles (dash-dotted lines). The vertical solid line in gray indicates the position within which gas density is above 10^5 cm^{-3} for each core. The vertical dotted line mark the effective radius of the obtained T_{kin} map from fitting the NH_3 (1,1) and (2,2) lines.

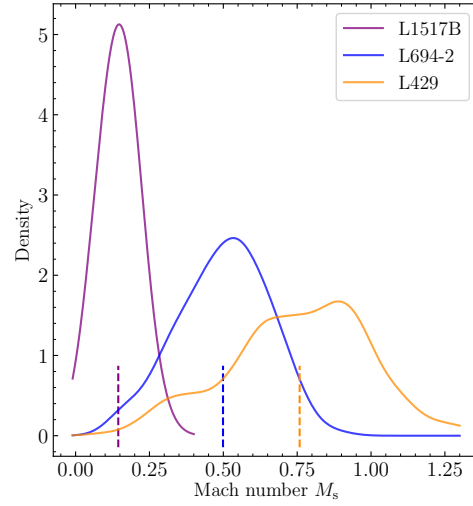


Fig. 12. The KDE of the Mach number of the three cores. The mean values are indicated with vertical line segments of respective colors.

Appendix A: Target sources

L694-2

L694-2 is a relatively isolated pre-stellar core (Lee & Myers 2011, Spezzano et al. 2016). Based on *Gaia* Data Release 2 astrometric data, the new distance of L694-2 is updated to 203 pc (Kim et al. 2022). Observations of N_2H^+ (1-0), DCO^+ (2-1) and HCO^+ (3-2), (4-3) lines all show blue-skewed profiles, which suggest infall motions from the extended region down to the inner core area (Williams et al. 2006, Keown et al. 2016, Kim et al. 2022). Compared to the proto-typical late-stage pre-stellar core L1544 (Keto & Caselli 2010, Caselli et al. 2019, 2022), its density gradient is smaller (Williams et al. 2006), with larger infall velocities associated with outer layers (Keown et al. 2016). These indicate L694-2 is a less evolved pre-stellar core than L1544. In addition, the core appears to be elongated and its density profile analysis based on near-infrared extinction suggests that it is likely a prolate structure with the major axis slightly inclined with respect to the line of sight (Harvey et al. 2003). L694-2 has an embedding cloud that appears to be filamentary and evidence of gas flows originated from the parental cloud that feed the core has been found (Kim et al. 2022).

L429

L429 is a late-stage pre-stellar core that holds high deuterium fraction among samples of starless cores (Crapsi et al. 2005, Bacmann et al. 2003, Caselli et al. 2008). The core is likely associated with the Aquila Rift, located at a distance of 436 pc (Ortiz-León et al. 2018). It appears to be a dark, absorption feature even at $70\mu\text{m}$, reflecting that very dense gas is residing within the core, which may be already collapsing if there is not strong magnetic field support (Stutz et al. 2009). This is compatible with the tentative infall signatures shown in the CS (3-2) line (as L429-1 in the survey of Lee et al. 2004) and HCN (1-0) line (Sohn et al. 2007). However, red-skewed line profile of CS lines are also detected towards the core (Lee & Myers 2011); according to the evolutionary sequence drawn by Lee & Myers (2011), L429 is marked as an intermediate evolutionary stage, between L1517B and L694-2, showing expanding motions when a static core is being perturbed.

L1517B

L1517B is a starless core located in the molecular cloud Taurus-Auriga cloud (Elias 1978, Galli et al. 2019), which is close to a state of thermal equilibrium (Crapsi et al. 2005, Tafalla et al. 2004, Kirk et al. 2006). The chemical modeling of Maret et al. (2013) suggests the core is at an evolved stage that may quickly collapse to form a protostar. Single-dish observations towards L1517B reveal systematically red-skewed line profiles (Tafalla et al. 2004, Sohn et al. 2007, Fu et al. 2011). Analytical works of Fu et al. (2011) suggest that L1517B is a typical core that shows coexistence of envelope expansion (or oscillating motions, e.g., Lou & Gao 2011) and core collapse, which produce the observed spectra. The deuteration fraction derived from N_2D^+ and H_2D^+ of L1517B is much lower than that of L429 and L694-2 (Crapsi et al. 2005, Caselli et al. 2008, Koumpia et al. 2020), indicating L1517B is at an earlier evolutionary stage than L429 and L694-2 (see also Schnee et al. 2013).

Appendix B: Derivation of the combined $850\mu\text{m}$ map

We retrieve the raw data of SCUBA2 $850\mu\text{m}$ of L429 and L694-2 from the Canadian Astronomy Data Center (CADC⁹) archive. SMURF software (Chapin et al. 2013) implemented in Starlink package¹⁰ is adopted for the data reduction. We use the Makemap command with the configuration file¹¹ suited for bright extended sources; compared to the parameters used for the generic pipeline products, a less aggressive spatial filtering of the raw map is conducted in the initial data cleaning to preserve the extended structures.

We extrapolate a $850\mu\text{m}$ flux map from SED of *Herschel* SPIRE data, and use this map as a model image to deconvolve the *Planck* image with Lucy-Richardson algorithm (Lucy 1974). The obtained deconvolved *Planck* image has an angular resolution close to the SPIRE $500\mu\text{m}$ image and preserves the flux level of the *Planck* image. The latter property is essential as the SCUBA2 maps suffer from different level of missing fluxes, which can be source sensitive, dependent on the observing weather condition and data reduction parameters. The deconvolved image which contains the extended emission structures is then combined with the SCUBA2 $850\mu\text{m}$ image in the Fourier domain using J-comb algorithm (Jiao et al. 2022). The method has proved to be superior than conventional linear image combination methods implemented in e.g. *immerge* in *miriad* and *feather* in *CASA*, by largely suppressing imaging defects inherent to the ground-based bolometric observations as well as conserving the high-resolution Gaussian beam pattern (Jiao et al. 2022). The obtained $14''$ combined $850\mu\text{m}$ map of L694-2 and L429 is shown in Fig. B.1. Applying the T_d map from SED of *Herschel* SPIRE data, we calculate the $N(\text{H}_2)$ map shown in Fig. B.2.

Appendix C: Comparison between adopted methods for the combination of VLA and GBT data

We adopt both the joint deconvolution method using *Miriad* and the model-assisted clean method using *CASA*, for the combination of VLA and GBT data. The last step of both methods is linearly adding the single-dish data with the previous, intermediate combined product in the Fourier domain with *feather* and *immerge* task implemented in each software. In particular, the mathematical form used in the *immerge* task ensures the total flux (within the primary beam) of the final combined image preserves that of the single-dish data (see e.g., Jiao et al. (2022)).

A thorough benchmark between the two methods, dependent on the input parameters (e.g., the weighting of the single-dish data in the first method) and the characteristics of the observational data (e.g, sparse or decent *uv* sampling of the interferometric data, overlapping scales between the single-dish and interferometric data, etc.), is beyond the scope of this paper. In what follows, we simply compare the fitted NH_3 column density ($N(\text{NH}_3)$) using the combined image products from the two methods, shown in Fig. C.1. We found there is no significant discrepancy or systematic bias of the two set of $N(\text{NH}_3)$ values, which means that the different combination approaches should

⁹ <https://www.cadc-ccda.hia-ihp.nrc-cnrc.gc.ca/en/>

¹⁰ The Starlink software (Currie et al. 2014) is currently supported by the East Asian Observatory.

¹¹ The `dimconfig_bright_extended.lis` file provided in SMURF package

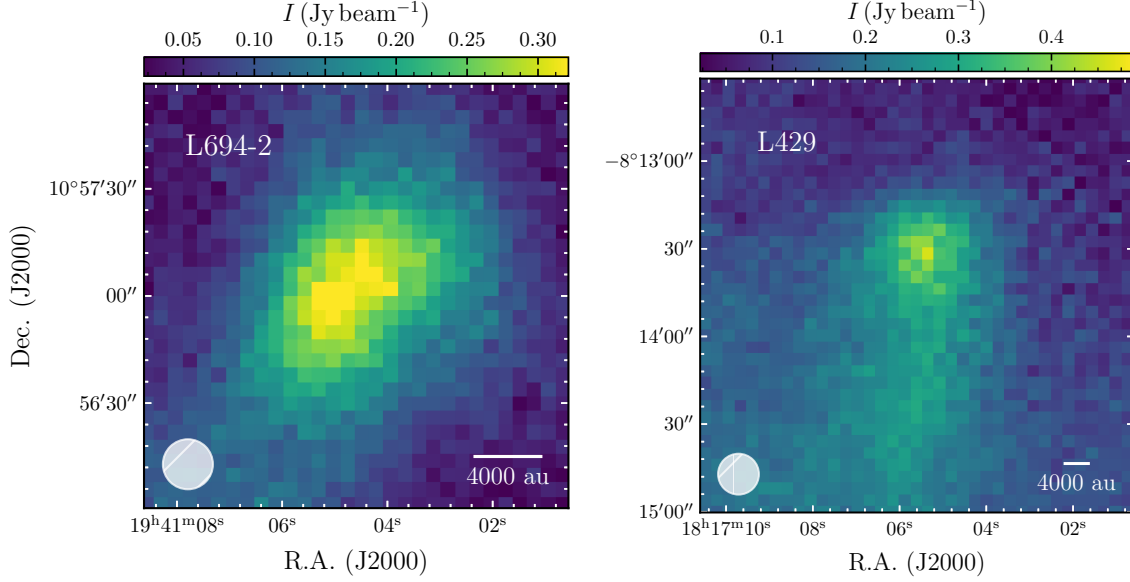


Fig. B.1. The 850 μm maps combining SCUBA2 850 μm and deconvolved *Planck* images, of L694-2 and L429.

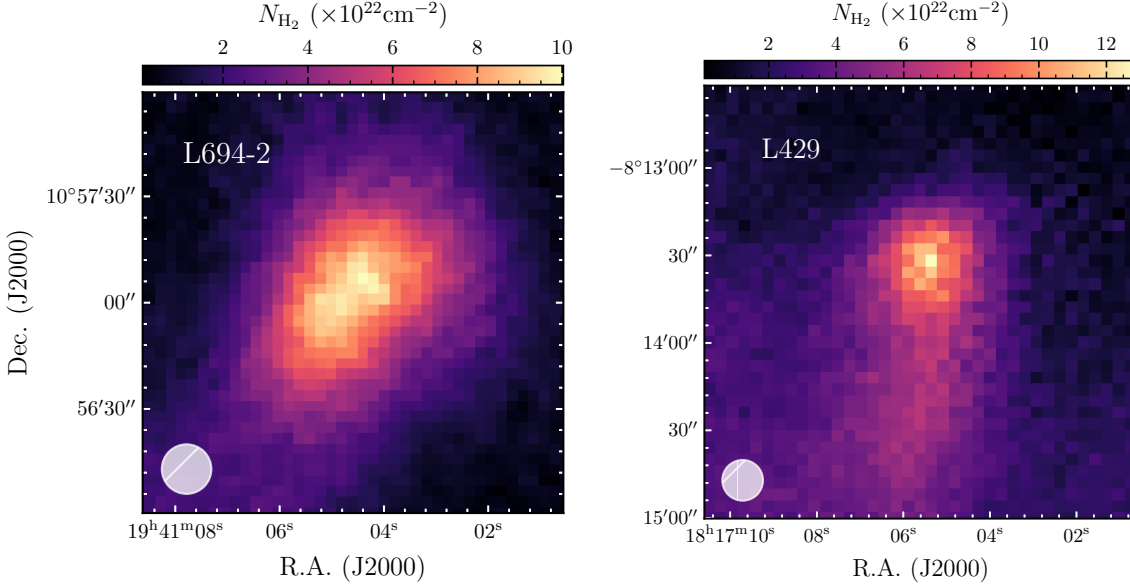


Fig. B.2. The 14'' hydrogen column density map derived from combined 850 μm map shown in Fig. B.1 and T_d map from SED of *Herschel* data.

not affect the analysis and comparison of our results with respect to Pineda et al. (2022).

Appendix D: Derivation and uncertainty of $N(\text{H}_2)$

We use the SMF method in Butler & Tan (2009) for background emission level estimates. After testing a set of different sized filters, we settled with a filter size of 90'', which minimizes the visual defect of interpolation while still preserving the median- to large-scale background emission pattern. The difference of the average background emission level for a filter size ranging between 60-270'' is within 10%.

Practically, the assumption of constant foreground emission level can cause underestimation of the column densities particularly in the outer parts of the core. By inspecting the 8 μm map and the contours of $N(\text{H}_2)$ map from *Herschel* it is obvious that some bright 8 μm emission is associated with the foreground of

the source. The small-scale median filter method effectively removes all contribution from compact bright sources for interpolation at the core area, ignoring the fact that there may be a bunch of stars that compose the background of the cores. The uncertainties associated with back- and foreground emission level estimates are hard, if not impossible, to assess. We resort to matching the τ profiles from the extinction method and from that the SED by a constant scaling factor. This is based on essentially the assumption that the morphological features of the $N(\text{H}_2)$ map derived by the extinction method, preserve the real profiles of the core structure without spatially varying degrees of deficit. This is largely based on what we find empirically, the constant scaling up can match the column density cuts along the core for the inner part and outer part simultaneously. The comparison between the profiles of original $\tau_{8\mu\text{m}}$ and that predicted from $\tau_{850\mu\text{m}}$ are shown in Fig. D.1, together with the scaled-up $\tau_{8\mu\text{m}}$.

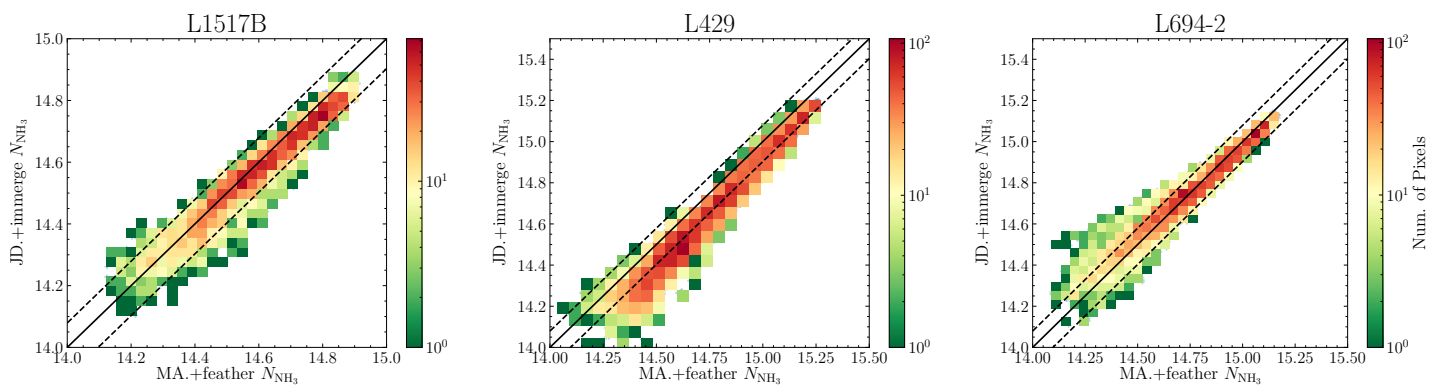


Fig. C.1. 2D histogram of comparison between fitted $N(\text{NH}_3)$ of different combined data products: one based on joint-deconvolution (JD) and immerge using *Miriad* and the other model-assisted (MA) multi-scale clean plus feather using *CASA*. The diagonal dashed and solid lines indicate a factor of 1.2, 1 and 0.8 difference.

Comparing the ratios between the scaled-up $\tau_{8\mu\text{m}}$ and that predicted from $\tau_{850\mu\text{m}}$, the consistency of ~ 1 can be achieved for most of our interested core area. Practically, the assumption of constant foreground emission level can cause underestimation of the column densities particularly in the outer parts of the core. By inspecting the $8\mu\text{m}$ map and the contours of $N(\text{H}_2)$ map from *Herschel* it is obvious that some bright $8\mu\text{m}$ emission is associated with the foreground of the source. The column densities in the whole core may also be underestimated if the background level estimate is too low. The small-scale median filter method effectively removes all contribution from compact bright sources for interpolation at the core area, ignoring the fact that there may be a bunch of stars that compose the background of the cores. The uncertainties associated with back- and foreground emission level estimates are hard, if not impossible, to assess. We resort to matching the τ profiles from the extinction method and from that the SED by a constant scaling factor. This is based on essentially the assumption that the morphological features of the $N(\text{H}_2)$ map derived by the extinction method, preserve the real profiles of the core structure without spatially varying degrees of deficit. This is largely based on what we find empirically, the constant scaling up can match the column density cuts along the core for the inner part and outer part simultaneously. The comparison between the profiles of original $\tau_{8\mu\text{m}}$ and that predicted from $\tau_{850\mu\text{m}}$ are shown in Fig. D.1, together with the scaled-up $\tau_{8\mu\text{m}}$. Comparing the ratios between the scaled-up $\tau_{8\mu\text{m}}$ and that predicted from $\tau_{850\mu\text{m}}$, the consistency of ~ 1 can be achieved for most of our interested core area.

As a simple sanity check, we derive the foreground image of $8\mu\text{m}$, using the scale-up $2''$ column density map, and assume the background image estimated from SMF is relatively robust. The level of the derived foreground image, compared to the constant I_{fg} we assumed, is a factor of 1.0-1.6 times higher for the pixels in the core area. This is a reasonable difference in terms of possible underestimates of the foreground emission level.

In fact, the deficit of the derived $N(\text{H}_2)$ (after smoothing) compared to that derived from SED of *Herschel* data can have different origins. For the outer parts of the core, it is mainly the intrinsic problem of extinction method being not sensitive to lower column density regime due to the way fore- and background emission level are estimated; for the central part of the core, there is possible variation of the dust opacities due to grain growth at high density. Specifically, we use the thin ice mantle without coagulation according to the models of Ossenkopf & Henning (1994), while the ratio of $\frac{\kappa_{8\mu\text{m}}}{\kappa_{850\mu\text{m}}}$ can be lower to 50%

with dust coagulation and thicker ice layers Ossenkopf & Henning 1994. This change of dust opacities can reconcile the less than 1.5 times underestimated $N(\text{H}_2)$ from $8\mu\text{m}$ extinction, but is expected to be most significant in the central ~ 1000 au region (e.g. Chacón-Tanarro et al. 2019).

The scaling factor of L1517B and L694-2 are 1.5 and 1.8, for L429 it is ~ 2.5 . This suggests that L429 is missing the most gas column densities from the extinction method. Indeed, the ambient cloud structure of L429 shows highest level of gas column densities, reaching $5 \times 10^{22} \text{ cm}^{-3}$ as seen from the *Herschel* map.

The uncertainty of $N(\text{H}_2)$ which comes from the dust grain scattering (main aggregates) and possible emission at $8\mu\text{m}$ (Lefèvre et al. 2016, Steinacker et al. 2005) is negligible ($\sim 0.1 \text{ MJy sr}^{-1}$) compared to the uncertainty of the background and foreground emission level estimates (Pineda et al. 2022), for a source with extended sky brightness of several times of 1 MJy sr^{-1} at $8\mu\text{m}$. We note that this is the case for all the three cores in our sample.

Appendix E: T_{kin} derived from VLA-only datacubes

In Crapsi et al. (2007), the temperature drop towards L1544 is revealed by the temperature map derived from VLA-only datacubes of NH_3 (1,1) and (2,2) lines. This means that the extended structure is missing, which presumably affects the emission of the low lying energy levels most, since these can be excited at lower density layers. The extent and degree of the missing extended structure is hard, if not impossible, to predict. We tested fitting the NH_3 models with the VLA-only NH_3 (1,1) and (2,2) lines and compare the distribution of T_{kin} vs. $N(\text{NH}_3)$ (as in Fig. 6, left panel) in Fig. E.1. Compared to results derived from combined data cubes, a large difference is seen towards L1517B, which shows an overall lower temperature of $\lesssim 8$ K, close to that towards L429 and L694-2. With VLA-only data, still there is not a significant temperature drop of the three cores as that revealed towards L1544. The temperature variations of L429 in the VLA-only data are even more flattened than that in the combined data. This shows that the slight temperature drops seen in the combined data towards L429 and L1517B are mainly associated with (the LOS weighting of) outer gas layers of the core, where the region under influence of radiation field is better preserved.

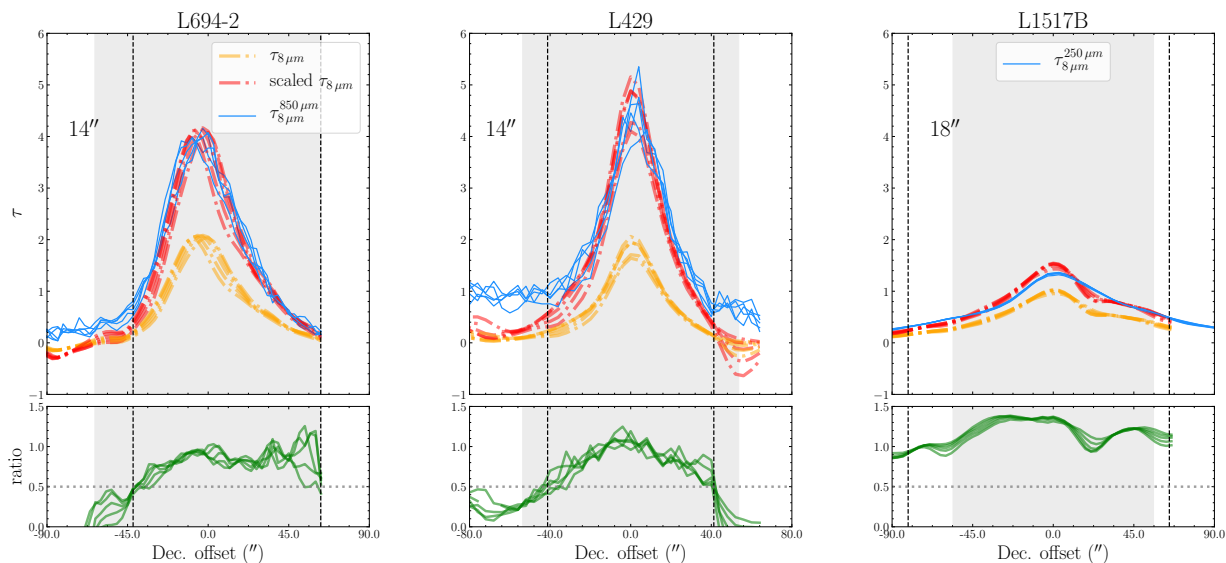


Fig. D.1. Comparison between profiles (along Declination) of opacity maps, extracted from original $\tau_{8\mu\text{m}}$ map, and that predicted from $\tau_{850\mu\text{m}}$ (denoted as $\tau_{8\mu\text{m}}^{850\mu\text{m}}$) or $\tau_{250\mu\text{m}}$ in the case of L1517B, and the scaled-up $\tau_{8\mu\text{m}}$ map. The two versions of $\tau_{8\mu\text{m}}$ map are both smoothed to 14" (18") to match the angular resolution of the $\tau_{850\mu\text{m}}$ ($\tau_{250\mu\text{m}}$) map. The lower panel shows the ratios between scaled-up $\tau_{8\mu\text{m}}$ and $\tau_{8\mu\text{m}}^{850\mu\text{m}}$ ($\tau_{8\mu\text{m}}^{250\mu\text{m}}$). Gray shaded region indicates the effective radius of the final trimmed parameter maps of NH_3 . Vertical dotted lines show the offset where the ratio drops below 0.5 (indicated by the horizontal dotted line).

Appendix F: Sub-regions with secondary velocity component

As stated in Sect. 3.3, for sub-regions of L694-2 and L429, there is evidence of a secondary velocity component. We present the two-component velocity and line-width maps in Figs. F.1 and F.4 and the example spectra across the sub-regions that have two or one velocity component in Figs. F.2, F.3, F.5, F.5. When generating the parameter maps, for the vast region where one-component fit is statistically preferred, the fitted values from this fit are assigned to corresponding pixels. In Figs. F.1-F.4 sub-regions showing two velocity components are marked by closed contours. These sub-regions are selected based on $\ln K_1^2$ threshold and trimmed according to fitted errors. Compared to trimming the one-component fit in Sect. 3.3, we used a less tight criteria: uncertainties of T_{kin} or T_{ex} larger than 2 K, v_{LSR} or σ larger than four channel widths (0.4 km s^{-1}).

Examining Fig. F.4 and Fig. F.1, it is clear that the sub-regions showing a secondary velocity component are where there are abrupt changes of the one-component velocity map. Comparing the two-component velocities with the one-component velocity of the main regions across the core, mostly, the velocity component that has a larger line-width seems to show a better consistency with main regions. The red-shifted, smaller line-width sub-regions connect to the outermost region of the core, which is clearer in the case of L429.

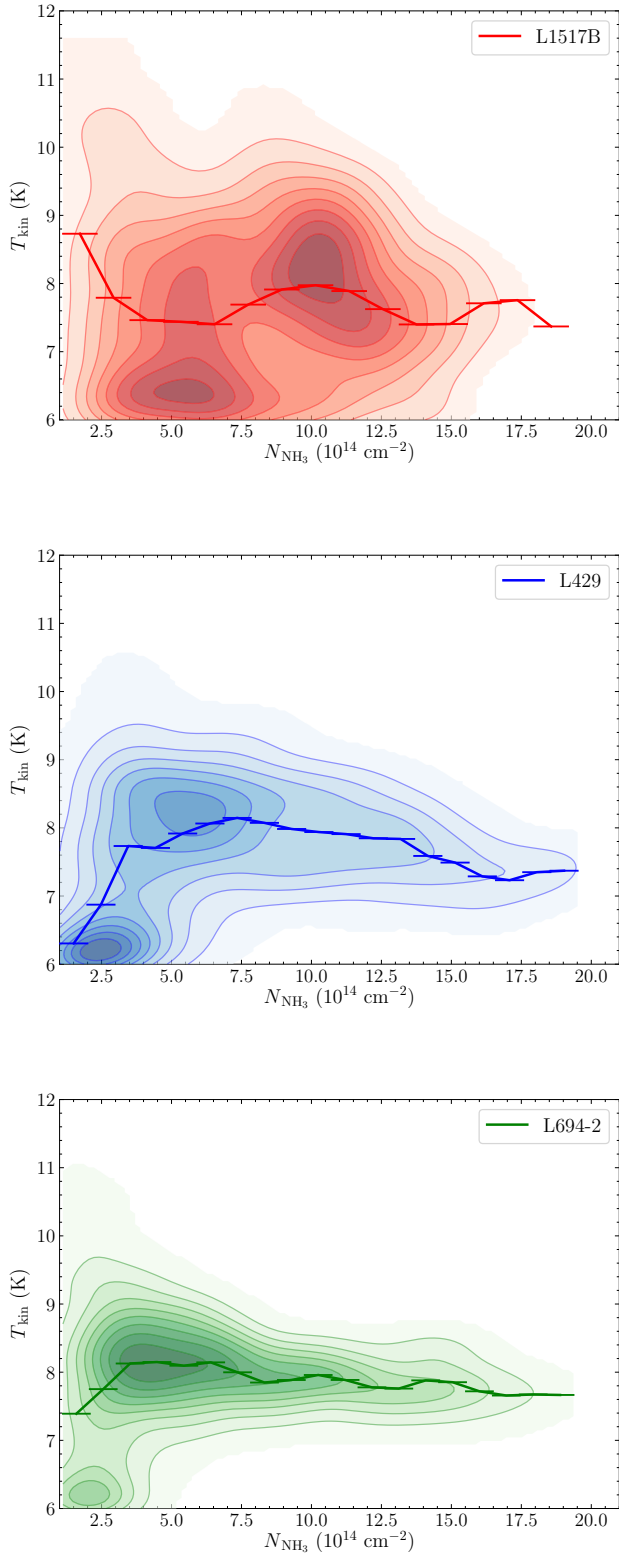


Fig. E.1. Kinetic temperature as a function of NH_3 column density for the three cores. Both quantities are derived from VLA datacube without combination with GBT data (as compared to right panel of Fig. 6). The line segments correspond to mean values in H_2 column density bins, which are linked together.

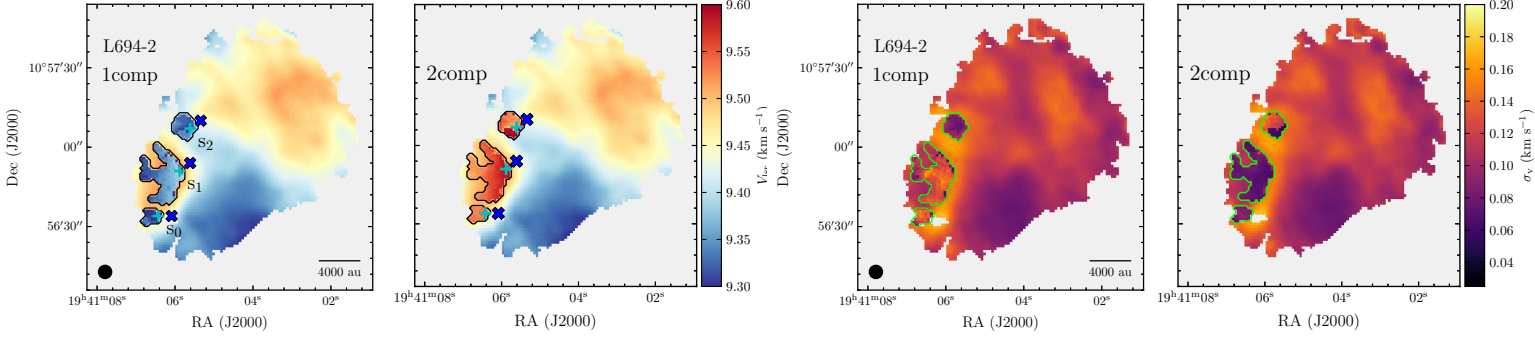


Fig. F.1. The velocity and line-width maps of L694-2 combining sub-regions where a secondary velocity component exist and the rest regions showing only one velocity component. The two-component sub-regions are enclosed by contours, defined by $\ln K_1^2$ and goodness of fit.

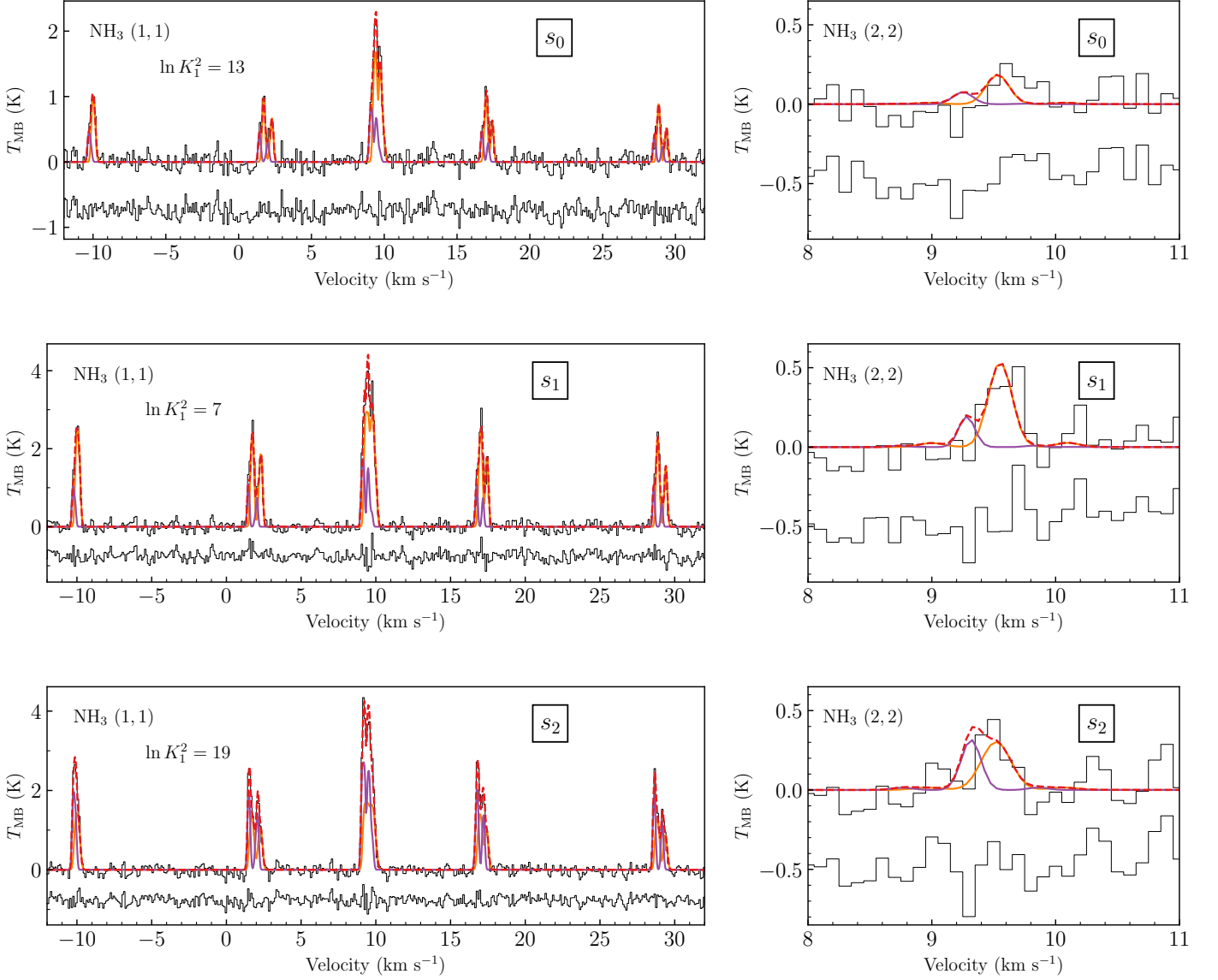


Fig. F.2. Example of two-component spectra towards s_1 , s_2 and s_3 regions of L694-2 as in Fig. F.1 (cyan pluses), of the NH_3 (1,1) and (2,2) lines. Red dashed lines show the overall two-component fit; orange and magenta lines shows the two component separately. The offset spectra show the residual of observed spectra minus the two-component model spectra.

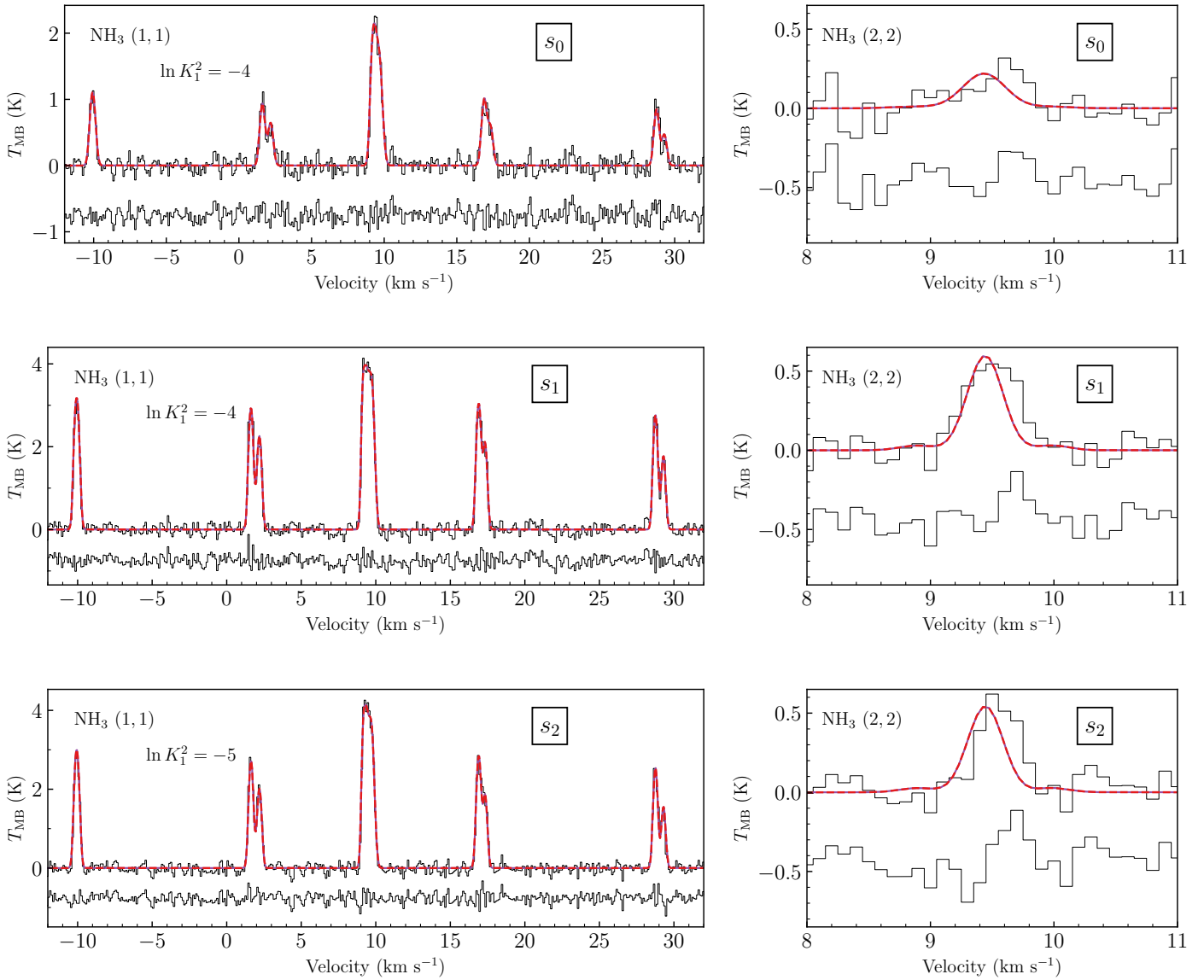


Fig. F.3. Same as Fig. F.2, but of the spectra in the inner region of s_1 , s_2 and s_3 (blue crosses in Fig. F.1) that only show one velocity component.

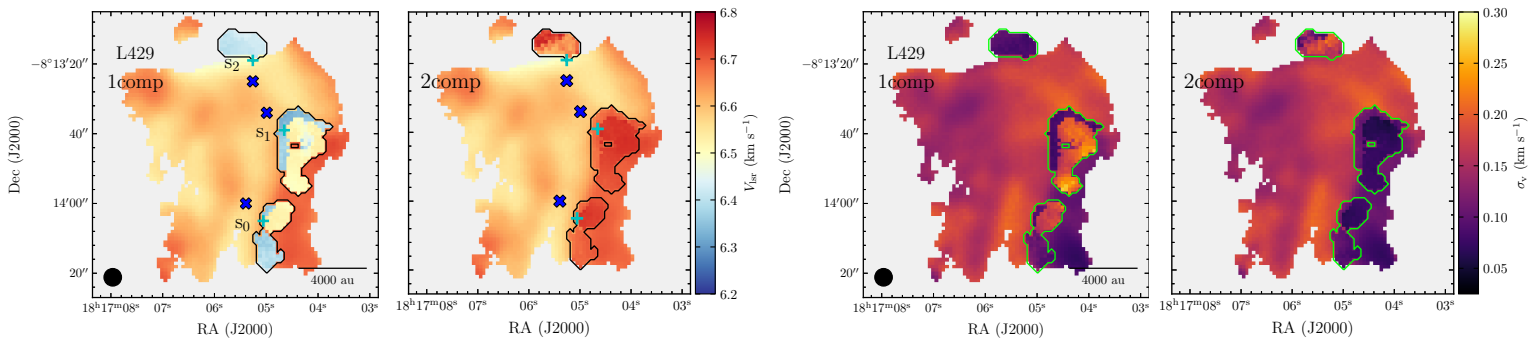


Fig. F.4. Same as Fig. F.1, but for core L429.

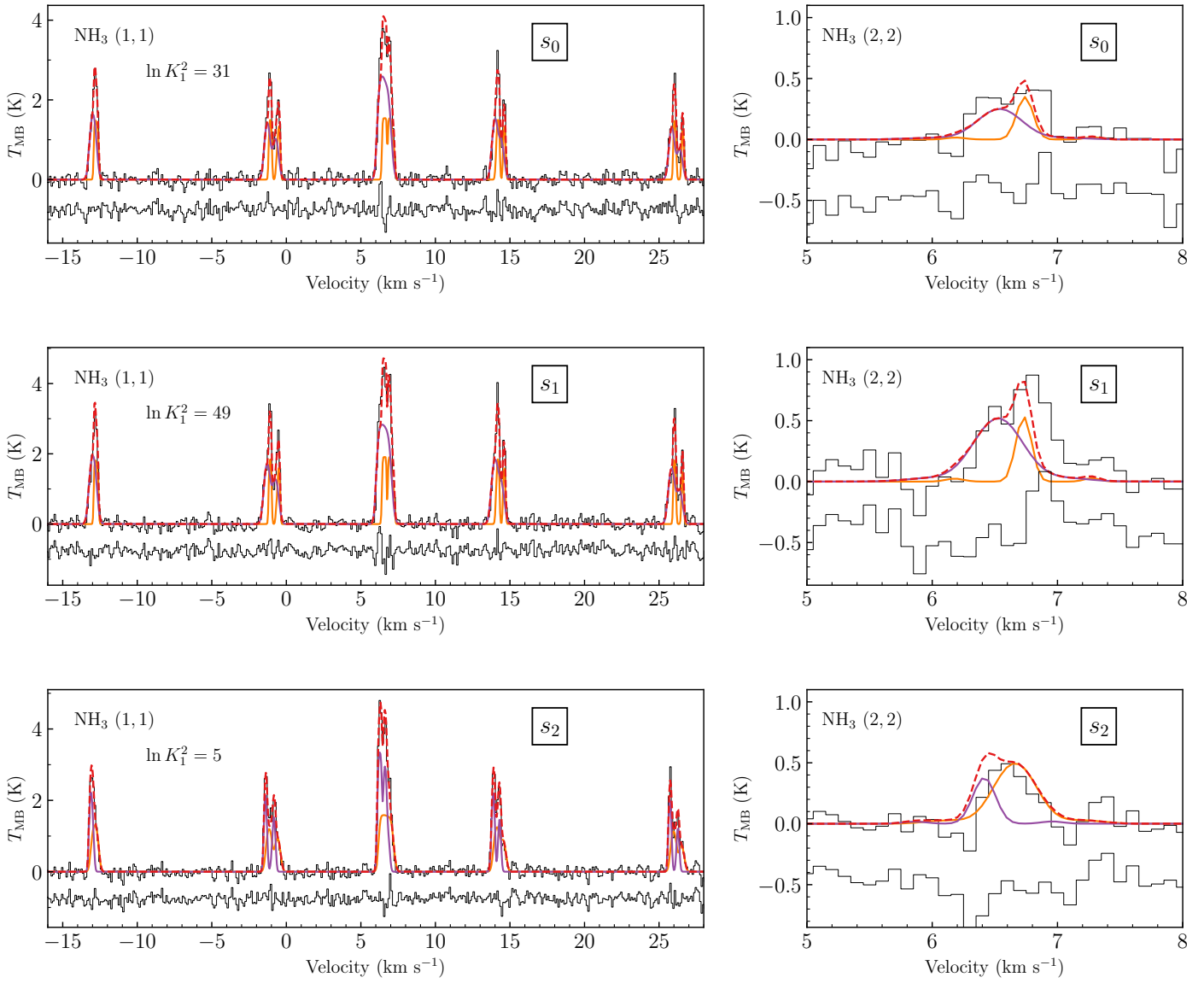


Fig. F.5. Same as Fig. F.2, but of core L694-2.

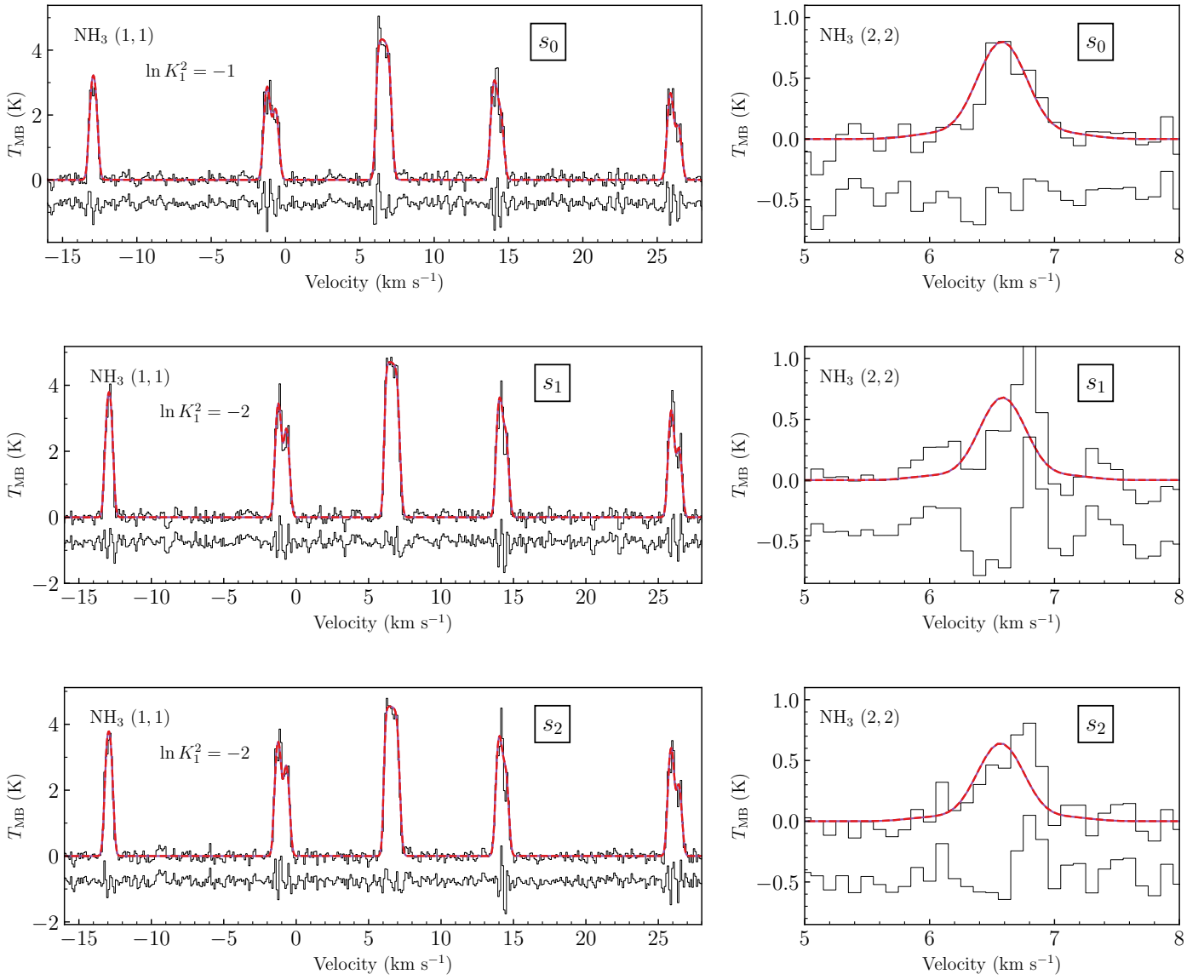


Fig. F.6. Same as Fig. F.3, but of the core L429.